The Physics of Heat Waves: What Causes Extremely High Summertime Temperatures?

LUCAS R. VARGAS ZEPPETELLO,[a] DAVID S. BATTISTI,[a] AND MARCIA B. BAKER[b]

[a] *Department of Atmospheric Sciences, University of Washington, Seattle, Washington*
[b] *Department of Earth and Space Sciences, University of Washington, Seattle, Washington*

ABSTRACT: We analyze observations and develop a hierarchy of models to understand heat waves—long-lived, high temperature anomalies—and extremely high daily temperatures during summertime in the continental extratropics. Throughout the extratropics, the number of extremely hot days found in the three hottest months is much greater than expected from a random, single-process model. Furthermore, in many locations the temperature skewness switches from negative on daily time scales to positive on monthly time scales (or shifts from positive on daily time scales to higher positive values on monthly time scales) in ways that cannot be explained by averaging alone. These observations motivate a hierarchy of models of the surface energy and moisture budgets that we use to illuminate the physics responsible for daily and monthly averaged temperature variability. Shortwave radiation fluctuations drive much of the variance and the negative skewness found in daily temperature observations. On longer time scales, precipitation-induced soil moisture anomalies are important for temperature variability and account for the shift toward positive skewness in monthly averaged temperature. Our results demonstrate that long-lived heat waves are due to (i) the residence time of soil moisture anomalies and (ii) a nonlinear feedback between temperature and evapotranspiration via the impact of temperature on vapor pressure deficit. For most climates, these two processes give rise to infrequent, long-lived heat waves in response to randomly distributed precipitation forcing. Combined with our results concerning high-frequency variability, extremely hot days are seen to be state-independent filigree driven by shortwave variability acting on top of longer-lived, moisture-driven heat waves.

KEYWORDS: Extreme events; Atmosphere-land interaction; Hydrometeorology

1. Introduction

Extremely high near-surface air temperatures can have deleterious consequences for human health, agriculture, and ecosystems. Recent work on daily temperature fluctuations in extratropical continental regions during summertime has focused on (i) the local insolation incident at the surface associated with stochastic variability in cloudiness (Meehl and Tebaldi 2004; Van Weverberg et al. 2018) and (ii) warm and cold air advection associated with synoptic motions (Schneider et al. 2015; Tamarin-Brodsky et al. 2020). Extremely hot days have been attributed to sunny skies acting in concert with site-specific synoptic circulation anomalies (e.g., warm air advection, subsidence associated with downslope winds, or a local high pressure system) that enhances warming driven by excess insolation (Bumbaco et al. 2013; Loikith et al. 2018; Linz et al. 2018). On time scales longer than one day, fluctuations in summertime temperature have been attributed to stochastic variations in (i) insolation incident at the surface and (ii) soil moisture associated with precipitation events (Koster et al. 2015; Vargas Zeppetello et al. 2020a). Many studies have pointed out that in continental regions, there is a strong relationship between meteorological droughts (i.e., extended periods of precipitation deficit) and high temperature anomalies that persist for weeks or months at a time during summer (e.g., Fischer et al. 2007; Miralles

et al. 2018; Wehrli et al. 2019). Given these varying explanations for different time scales of summertime temperature variability and the societal importance of extremely high temperatures, we examine the physical processes responsible for the variance and skewness of temperature on daily and monthly time scales and seek in particular to illuminate how different time scales of variability contribute to the events conventionally referred to as heat waves and extremely hot days (see the *AMS Glossary of Meteorology* definition at https://glossary.ametsoc.org/wiki/Heat_wave; Perkins and Alexander 2013).

We define an *extremely hot day* as one in which the daily maximum temperature exceeds the local 95th temperature percentile for the summer months in the Northern Hemisphere [June, July, and August (JJA)]. To probe the connection between daily and monthly temperature variability, Fig. 1a shows the "extreme concentration" N_e defined as the total number of extremely hot days that occurred during the three hottest summer months at each extratropical grid box (north of 25°N) during the period 1985–2014 (see section 2 for details on the data used in this study). Typically, $N_e \sim 30$ across the extratropics ($10 \leq N_e \leq 55$). To understand whether observed N_e can be explained by random variations in daily temperature, we examine numerical experiments with autoregressive models of order one (AR1), where the noise applied to the model is independent of the model state. By varying the autocorrelation coefficient r in the AR1 models, we derived an empirical relationship for N_e as a function of r. We then calculated r for each grid box in Fig. 1a (typically
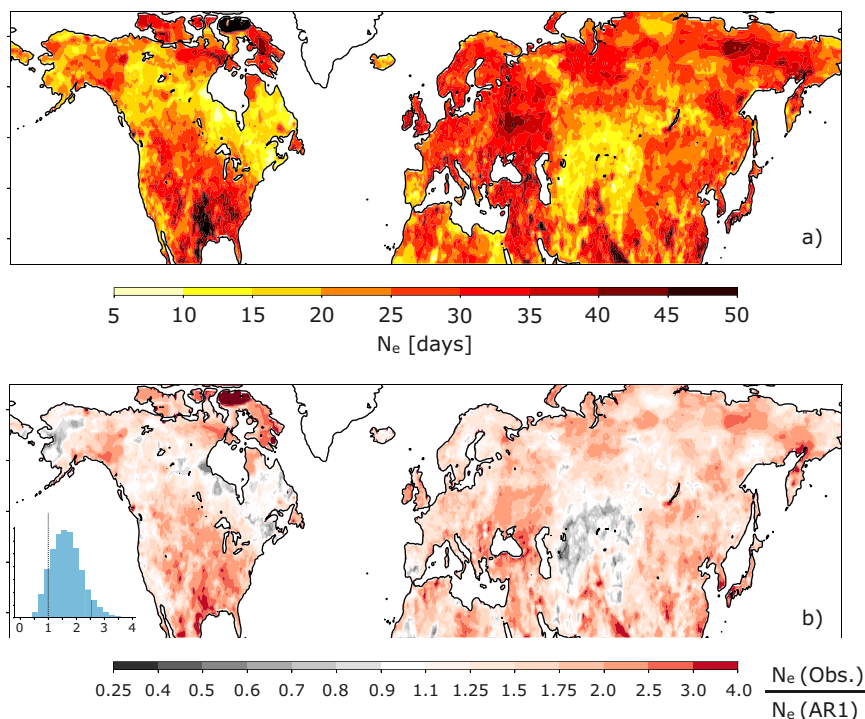
FIG. 1. (a) The "extreme concentration" N_e defined as the number of extremely hot days in the hottest three summer (JJA) months of the historical record (see section 2a for details on datasets). (b) The ratio of observed N_e to N_e expected from an AR1 process with the observed one-day autocorrelation coefficient in temperature from each grid box. The inset in (b) shows an area-weighted histogram summarizing the ratio across the extratropics.

$0.5 \le r \le 0.7$) and used our empirical $N_e(r)$ relationship to compute the extreme concentration expected across the extratropics if daily temperatures were an AR1 process with the observed (local) autocorrelation coefficient. The ratio of N_e found in observations to $N_e(r)$ expected from our AR1 numerical experiments is shown in Fig. 1b; a value of one indicates that observed N_e can be explained by an AR1 process. Observed N_e is 50% greater on average than expected from an AR1 process (see histogram inset in Fig. 1b for a summary of this ratio across the extratropics). The finding that extremely hot days are inordinately highly clustered in the three hottest months of the historical record throughout the extratropics suggests that understanding low-frequency temperature variability is the foundation for understanding extremely hot days.

To explain why N_e is higher than expected from a simple autoregressive process, we need to understand the shape of the probability distribution of summertime temperatures. Figure 2 shows the variance and skewness of daily maximum (Figs. 2a,b) and monthly average (Figs. 2c,d) observed 2-m air temperature distributions. The contours in Figs. 2b and 2d show places where the skewness is statistically distinguishable from zero. Methods for removing the seasonal cycle and the robustness of the statistics presented in Fig. 2 are discussed in section 2a. Throughout this study, we will use the statistics of daily maximum and monthly average temperatures as proxies for high- and low-frequency variability, respectively.

The amplitude of the monthly average temperature variance is reduced by a factor of 10 on average compared to the daily maximum temperature variance (cf. Figs. 2a,c and note the different color bars). This ratio of daily to monthly temperature variance is similar to what is expected from the AR1 experiments with decay time scales set by the observed one-day autocorrelation coefficient. Furthermore, the spatial pattern of daily maximum temperature variance is very similar to that of monthly average temperature variance (the pattern correlation of Figs. 2a and 2c is $r = 0.70$). In our numerical experiments with randomly distributed daily temperatures, we found that daily and monthly average variance were well correlated and that the ratio of daily to monthly average temperature variance was close to 10:1 for autocorrelation coefficients similar to those found across the extratropics.

As a demonstration of the applicability of an AR1 model to describe observed temperature probability density functions (PDFs), Fig. 2e shows temperature PDFs for a location in eastern Europe (blue star in Figs. 2a–d): the observed daily maximum PDF is shown by a solid blue line and a PDF generated by an AR1 model with the same autocorrelation coefficient as the eastern European daily observations and noise amplitude tuned to match the daily temperature variance is shown by a dashed blue line. The dashed orange line shows the PDF generated by taking monthly averages of output from the AR1 model, the solid orange line shows the PDF
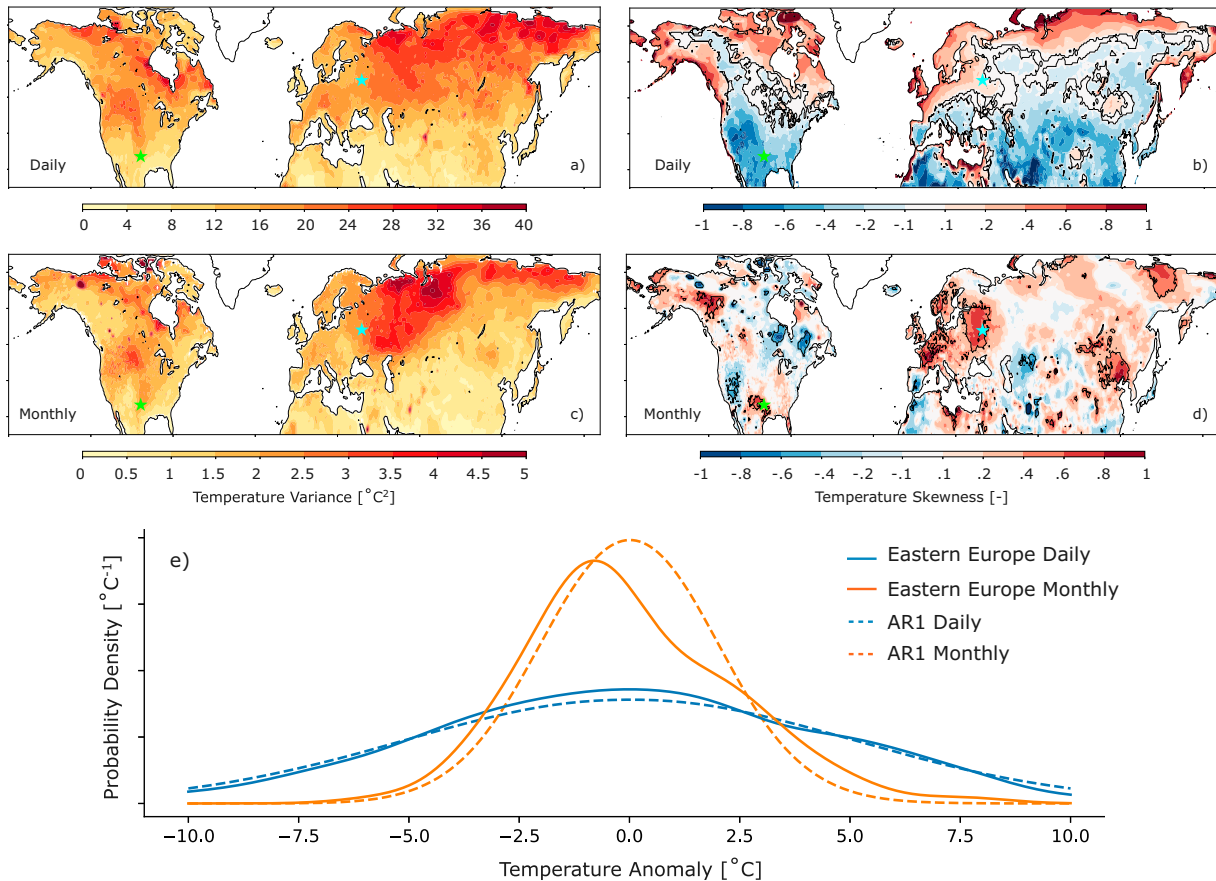
FIG. 2. (a),(b) Daily and (c),(d) monthly temperature (left) variance and (right) skewness for JJA 1985–2014. Contour lines in (b) and (d) show regions where the skewness is statistically distinguishable from zero (see section 2a). Stars show places with increasingly positive temperature skewness on longer averaging time scales that will be investigated in this paper. (e) Probability density functions (PDFs) of observed daily (blue) and monthly average (orange) temperatures in eastern Europe [blue star in (a)–(d)] in solid lines; dashed lines show daily (blue) and monthly average (orange) temperature PDFs generated from numerical experiments with an AR1 process tuned to match the daily variance from the eastern European observations; 10 000 synthetic "summers" contribute to the dashed PDFs to eliminate the effects of sampling.

generated by taking monthly averages of the daily observations.

The AR1 model of daily temperature variance in eastern Europe captures the variance in monthly average temperature, but not the skewness, which is indistinguishable from zero in daily observations (and by definition in the white-noise–forced AR1 models) but positively skewed in the monthly averaged observations. This result is inconsistent with an AR1 model that assumes low-frequency variability is due to the same physical processes that are responsible for high-frequency variability (one memory time scale and additive noise). The *increasing* skewness at longer averaging time scales apparent in eastern Europe is not unique to this region. Over more than half of the extratropical land surface, the temperature skewness on monthly time scales either switches from negative on daily time scales to positive on monthly time scales (38% of land area) or increases from a positive value on daily time scales to a *higher* positive value on monthly time scales (14% of land area). Further, in

62% of the land area where daily temperature skewness is statistically distinguishable from zero, the distribution is negatively skewed (this corresponds to 51% of total land area), while in 79% of the land area where the monthly average temperature skewness is statistically distinguishable from zero, the distribution is positively skewed (this corresponds to 13% of total land area). In section 3, we show that stochastic variations in solar radiation play an important role in the negative skewness of daily average temperature distributions. The preponderance of positively skewed monthly average temperature distributions is even more surprising when the negatively skewed radiation forcing on the land surface is considered. Proistosescu et al. (2016) found that the skewness of an AR1 process driven by skewed additive noise *decays* toward zero as the averaging time scale increases; this also follows directly from the central limit theorem. The distinctions between this result and observed summertime temperature distributions on daily and monthly time scales suggest that the processes

responsible for low-frequency variability are different from those that are responsible for high-frequency variability.

In section 2 (after summarizing the datasets used in this study), we develop a 1D model of surface temperature and soil moisture starting from the surface energy and moisture budgets, the Surface Energy and Moisture Budget Model (SEMB), then use locations in the central United States and eastern Europe (denoted by the green and blue stars, respectively, in Figs. 2a–d) as case studies to evaluate the model. Both of these case study regions exhibit a transition toward positive skewness at longer averaging time scales (see stars in Figs. 2a–d). In section 3, we examine the statistics of observed shortwave radiation variability and use the SEMB to demonstrate that variability in the flux of shortwave radiation (i.e., cloudiness or surface albedo; Van Weverberg et al. 2018) plays an important role in determining observed patterns of temperature variance and predominantly negative temperature skewness on daily time scales. In section 4, we apply the governing equations of the SEMB in steady state to show how the nonlinear relationship between evapotranspiration, soil moisture, and temperature impacts monthly average temperature skewness. In section 5, we apply the results of section 4 to formulate an even simpler "random precipitation" model to illuminate how summertime temperature variability is influenced by the average frequency of (random) precipitation events and other climate parameters. In section 6, we show how the moments of precipitation-induced variability of soil moisture and temperature depend on the background climate state. In section 7, we return to the observations of N_e and show that our theoretical framework for monthly temperature variability driven by randomly distributed precipitation events is extremely relevant for understanding individual extremely hot days across the extratropics. Conclusions about the clustering of extremely hot days in the hottest months of the historical record and the time scale dependence of temperature skewness are presented in section 8.

2. Methods

a. Data and reanalysis

We use daily maximum 2-m air temperature and total daily precipitation data from the Climate Prediction Center (CPC) for the years 1985–2014 and monthly average 2-m air temperature from Willmott and Matsuura (2018). In this study we focus on the extratropics, as these are the regions for which the most accurate data are available for the historical period, particularly for the United States and Europe. For temperature and all other quantities where anomalies are calculated, the seasonal cycle is removed. In monthly data, this process involves subtracting the respective monthly climatology from the particular month in question; in daily data, the same procedure was used to remove the seasonal cycle at each day except that the observed average seasonal cycle was smoothed with a low-pass filter. Similar results for skewness of daily maximum temperatures are found in Cavanaugh and Shen (2014) and McKinnon et al. (2016) using different methods to remove the seasonal cycle. Since only 90 (30 years

times 3 months per year) monthly values appear in our analysis, we examined three additional datasets to ensure the variance and skewness were insensitive to our choice of dataset: monthly averages of the daily CPC data, the monthly average 2-m air temperature data from the Berkeley Earth dataset (Rohde et al. 2013), and the monthly average temperature from the ERA5 reanalysis (Hersbach et al. 2020). The variance and skewness found in these datasets were in good agreement with those shown in Figs. 2c and 2d. We conducted 1000 resampling trials with 90% of the total data values each to generate the skewness maps shown in Figs. 2b and 2d. The standard deviation of skewness calculated from the samples was used to determine whether the local temperature skewness is statistically distinguishable from zero at the $p < 0.05$ confidence level and we followed Wilks (2016) to control for the false detection rate of spatially correlated data. Regions where skewness is significantly different from zero at this criterion are denoted by black contours in Figs. 2b and 2d.

Daily average surface absorbed shortwave radiation data are from the AVHRR satellite (Karlsson et al. 2012) and cover JJA 1995–2009. Monthly average absorbed shortwave radiation data are from the CERES satellite (Loeb et al. 2018) and cover 2000–17. To check for consistency in the datasets (as we did for the temperature data), we averaged daily observations from the AVHRR dataset for each month in the record and compared the resultant variance and skewness statistics to the CERES dataset. We found that statistics calculated from the AVHRR monthly averaged data agree well with those calculated from CERES over their common 2000–09 period. Finally, we used monthly mean near-surface specific humidity q and surface soil moisture m output from the ERA5 reanalysis spanning JJA 1985–2014.

b. The Surface Energy and Moisture Budget Model

Over land, the surface energy budget is

$$C \frac{dT}{dt} = F_{SW} - F_{LW} - LE - H_s - G. \qquad (1)$$

In Eq. (1), T is the land surface temperature, F_{SW} is the absorbed shortwave radiation, F_{LW} is the net upward surface longwave radiation, E is the evapotranspiration, H_s is the surface sensible heat flux, and G is the ground heat flux. The variable L is the latent enthalpy of vaporization [J (kg H_2O)$^{-1}$] and C is the surface heat capacity defined as

$$C = c_p \rho_s h, \qquad (2)$$

where c_p is the specific heat of the soil, ρ_s is the soil density, and h is the soil depth. The units for all terms in Eq. (1) are watts per square meter (W m^{-2}).

The moisture budget for the surface soil layer is

$$\mu \frac{dm}{dt} = P - E - R - I, \qquad (3)$$

where m measures the fraction of available soil pore space occupied by liquid water (m varies between zero and one); P is the precipitation rate, R is the runoff, and I is the infiltration

TABLE 1. Climatological values of absorbed shortwave radiation $\overline{F_{SW}}$, event average precipitation $\overline{P}$, dewpoint temperature T_D, and near-surface specific humidity $\overline{q}$ as well as the dry response parameter α and surface resistance r_s for the two case study regions (see stars in Fig. 2).

Region	$\overline{F_{SW}}$ (W m^{-2})	$\overline{P}$ (mm)	T_D (°C)	$\overline{q}$ [g H$_2$O (kg air)$^{-1}$]	α (W m^{-2} K^{-1})	r_s (s m^{-1})
United States	215	4.1	17	12	17	150
Europe	187	3.6	13	9	16	75

rate. The water holding capacity of the soil layer μ in Eq. (3) is given by

$$\mu = \rho_l h \theta_{max}, \qquad (4)$$

where ρ_l is the density of liquid water and θ_{max} is the fraction of the soil matrix that is accessible to liquid water. The units for all terms in Eq. (3) are kg H$_2$O m^{-2} s^{-1}.

Net longwave radiation, surface sensible heat flux, and the ground heat flux all respond to changes in surface temperature T. Linear regressions of surface temperature on these three energy fluxes explain most of their monthly variability despite the T^4 behavior of longwave radiation and the influence of other variables like atmospheric humidity and temperature or wind speed (see Vargas Zeppetello et al. 2020b). We assume that

$$F_{LW} + H_s + G = \alpha(T - T_D), \qquad (5)$$

where T_D is the local dewpoint temperature and α (W m^{-2} K^{-1}), the "dry response parameter," controls how effectively the longwave, sensible, and ground heat fluxes damp temperature anomalies in the absence of evapotranspiration. Our use of T_D as the model's reference temperature in Eq. (5) ensures that only positive evapotranspiration values are output from the model and that we simulate no condensation of dew.

We parameterize evapotranspiration as

$$E = \nu_L m [q_s(T) - \overline{q}], \qquad (6)$$

where the parameter $\nu_L = \rho_a/r_s$, where ρ_a is the density of near-surface air and r_s (s m^{-1}) is the effective surface resistance. The saturation specific humidity $q_s(T)$ is given by the Clausius-Clapeyron relationship and $\overline{q}$ is the climatological near-surface specific humidity. We neglect variations in q, which have been shown to be much smaller than variations in $q_s(T)$ that are due to fluctuations in surface temperature (van Heerwaarden et al. 2010). The linear dependence of E on m in Eq. (6) has been used since the earliest climate models (Manabe 1969) and captures the basic hydrological connection between soil moisture and evapotranspiration (Delworth and Manabe 1988). In previous work (Vargas Zeppetello et al. 2019), we have shown that Eq. (6) can accurately model the observed transition in evapotranspiration behavior across wet and dry soil moisture "regimes" provided that the surface energy budget equation [Eq. (1)] is coupled to the surface moisture budget [Eq. (3)].

Using Eqs. (5) and (6) and assuming that runoff and infiltration act only to impose an upper limit on surface soil moisture, we arrive at the following equations for the evolution of temperature and soil moisture that constitute the Surface Energy and Moisture Budget Model (SEMB):

$$C \frac{dT}{dt} = F_{SW}(t) - \alpha(T - T_D) - L\nu_L m [q_s(T) - \overline{q}], \qquad (7)$$

$$\mu \frac{dm}{dt} = P(t) - \nu_L m [q_s(T) - \overline{q}]. \qquad (8)$$

In the SEMB [Eqs. (7) and (8)], shortwave radiation F_{SW} and precipitation P are written as functions of time to denote that we use observations of these quantities as forcings on the land surface and assume that they are independent of the state variables T and m. While this assumption does not hold everywhere (Koster et al. 2004), it allows us to use daily shortwave radiation and precipitation data as inputs to the model and investigate the temperature response. The daily average downward shortwave radiation observations are multiplied by the climatological mean albedo to account for local variations in surface reflectance. The SEMB relies on three parameters: the soil column depth, set to be $h = 10$ cm; the surface resistance, which is governed by both surface properties and plant physiology; and the dry response parameter α (W m^{-2} K^{-1}), which is a function of regional mean temperature and soil moisture because it controls the magnitude of the net longwave and sensible heat fluxes.

c. Model evaluation: The SEMB control simulations

To verify the efficacy of the SEMB, we use the observed daily time series of shortwave radiation F_{SW} and precipitation P for 15 summers (JJA 1995–2009) from the two regions highlighted by stars in Fig. 2 as model forcings in Eqs. (7) and (8); these represent our *control simulations* for both regions. Values for α are taken from previous work that calculated linear regressions between the fluxes in Eq. (5) and surface temperature (Vargas Zeppetello et al. 2020b); these monthly regressions explicitly eliminate high-frequency variability in the longwave, sensible, and ground energy fluxes. The r_s parameter is tuned so that the mean temperature simulated by the SEMB matches that of the study region in question. The T_D values are calculated by using the Clausius–Clapeyron relationship to match the average specific humidity in the ERA5 reanalysis. The model is initialized with values of T and m, at each time step the fluxes are calculated, and then a finite-difference algorithm integrates the state variables forward in time. For all results presented here we used 60 time steps per day, but our results were not sensitive to this choice. Relevant climatological values and model parameters for both regions are shown in Table 1. We use the climatological averaged m and T from ERA5 reanalysis for the initial conditions in all simulations; statistics from the are not sensitive to the choice of initial conditions.
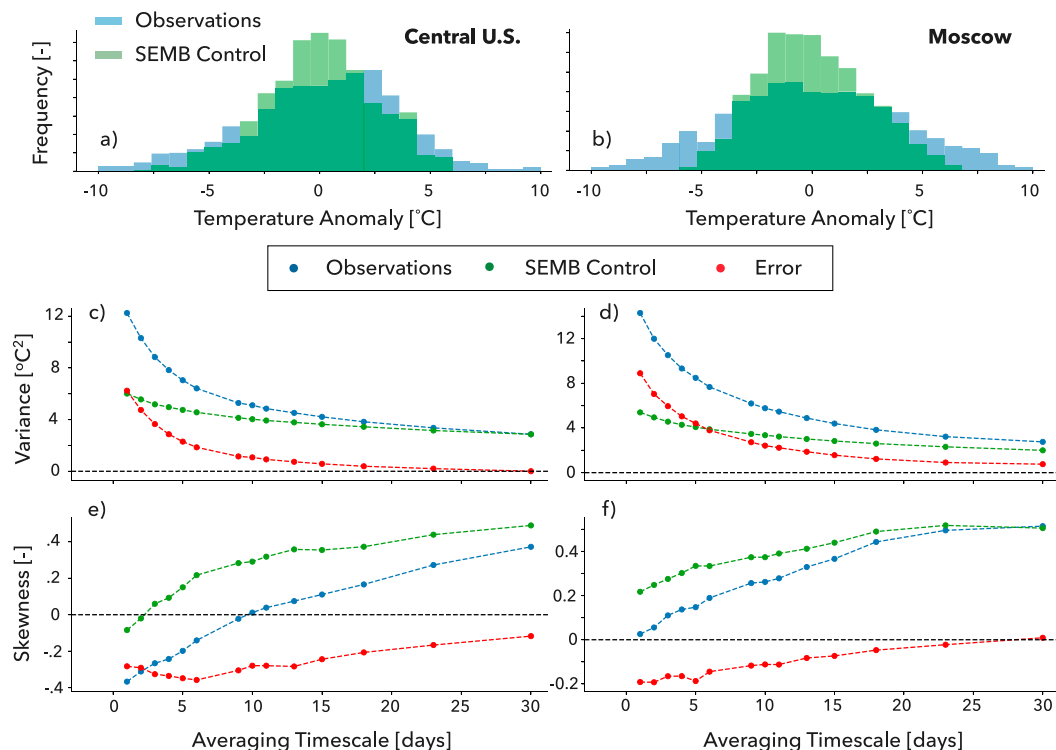
FIG. 3. Observations and model output for daily temperature anomalies over (left) the central United States and (right) eastern Europe (see stars in Fig. 2). (a),(b) Frequency distributions for anomalies in CPC observations (blue bars) and temperature output from the SEMB (green bars). Temperature (c),(d) variance and (e),(f) skewness are shown as a function of averaging time scale. Blue dots/lines show observed values from the CPC data. Green dots/lines show results from the SEMB control simulations. The differences between the observations and the SEMB control simulations are shown in the red dots/lines.

Before we present model results, we note two important caveats. First, we compare surface temperature from the to daily maximum 2-m air temperature observations. The correlation between existing gridded estimates of land surface and 2-m air temperature is generally greater than 0.9 outside the tropics (Good et al. 2017), suggesting that the variability in surface temperature output by the SEMB can be directly compared to the variability in observed maximum 2-m air temperature. Second, the SEMB is forced with daily average values of shortwave radiation and the resulting temperature is compared to observed daily maximum 2-m air temperature. Despite these inconsistencies between the model and the observations we compare it to, Figs. 3a and 3b show that the surface temperature variability simulated by the SEMB is similar to the variability in observed maximum 2-m air temperatures.

In Figs. 3c–f, the temperature variance (Figs. 3c,d) and skewness (Figs. 3e,f) are shown as functions of averaging time scale for the SEMB (green dots/lines) and the observations (blue dots/lines). The differences between observed and SEMB statistics are shown by red dots/lines. To create these plots, we sampled random continuous segments of varying lengths; each dot in Figs. 3c–f shows the average variance or skewness averaged across 5000 trials.

There is good agreement between the SEMB and observations, particularly on monthly time scales. When forced with observed daily radiation and precipitation, the SEMB features (i) a decrease in variance as the averaging time scale increases from one day to one month and (ii) an increasingly positive skewness at longer averaging time scales. The SEMB underestimates the high-frequency temperature variance in both study regions (see Figs. 3c,d); this is expected because thermal advection contributes to daily temperature variance and is not included as a forcing in our model. However, the SEMB more accurately simulates the variance on longer time scales; this suggests that advection is not a significant source of monthly average temperature variability in either region, consistent with the findings of Holmes et al. (2016) and Chan et al. (2020). Simplified versions of Eqs. (7) and (8) have been used to understand the monthly temperature variance across the extratropics in Vargas Zeppetello et al. (2020a).

At both sites, skewness increases as the averaging time scale increases in both the SEMB and the observations. Similar to the variance results, the skewness in the output from the SEMB agrees better with the skewness in the observations at longer averaging time scales. The differences between simulated and observed skewness in the shorter averaging time scales are likely due to variability driven by stochastic
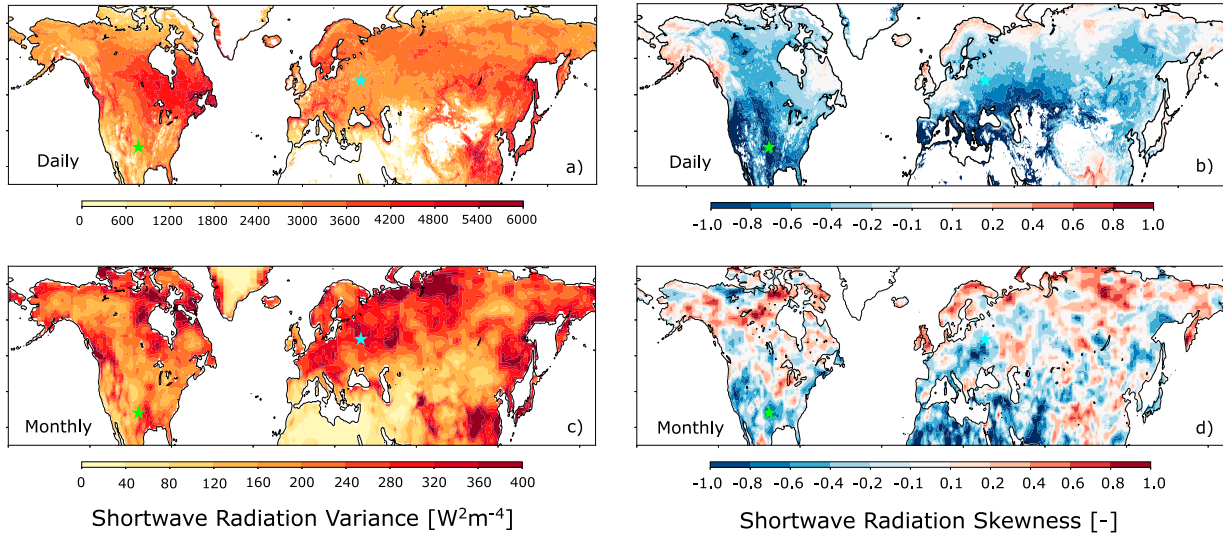
FIG. 4. (left) Variance and (right) skewness of absorbed surface shortwave radiation distributions in JJA. The (a),(b) daily data are from Karlsson et al. (2012) and are for 1995–2009, while the (c),(d) monthly data are from Loeb et al. (2018) and are for 2000–17.

variations in temperature advection that are not included in our model but may contribute to the negative skewness in temperature on daily time scales in these regions (Tamarin-Brodsky et al. 2020).

In the four sections that follow, we illuminate the impact of shortwave radiation and precipitation on land surface temperature variability to understand the processes responsible for the dependence of summertime temperature statistics on averaging time scale seen in the observations and simulated by the SEMB.

3. Radiation, precipitation, and temperature variability

a. Observations of radiation-induced temperature variability

Figure 4 shows the daily and monthly average absorbed shortwave radiation variance and skewness across the extratropics (note again the different color bars on the variance plots). On daily time scales, the skewness of surface shortwave radiation is strongly negative nearly everywhere, probably because insolation has an upper (clear sky) limit and clouds can only decrease the absorbed shortwave flux at the surface.

To quantify the contribution of shortwave radiation fluctuations to summertime temperature variability, we modify the SEMB to *exclude* the influence of soil moisture anomalies on the surface energy budget by prescribing a constant mean value of soil moisture $\overline{m}$ in Eq. (7). We expand shortwave radiation and temperature into a climatological mean value (barred terms) and anomalies about the climatology (primed terms); for temperature, $T = \overline{T} + T'$. Assuming that the climatology is in equilibrium, Eq. (7) becomes

$$C \frac{dT'}{dt} = F'_{\text{SW}} - \alpha T' - L\nu_L \overline{m}\gamma T'. \tag{9}$$

The value of $\gamma \equiv dq_s(T)/dT$ is calculated from the Clausius–Clapeyron relationship using observed local climatological surface temperature. While the temperature tendency term is important for understanding the diurnal cycle of surface temperature (Kleidon and Renner 2018), scale analysis shows that on time scales longer than one day, the time tendency term in Eq. (9) is small compared to terms on the right-hand side and can be ignored. Equation (9) then simplifies to

$$T' = \frac{F'_{\text{SW}}}{\alpha + L\nu_L \overline{m}\gamma}. \tag{10}$$

Equation (10) is similar to the model presented in Vargas Zeppetello et al. (2020a), but here soil moisture anomalies have been completely neglected. The diagnostic model [Eq. (10)] predicts that temperature anomalies are inversely proportional to mean soil moisture because a higher fraction of incoming energy is used to evaporate liquid water over wet soils than over dry soils; this effect has been noted in several previous studies (e.g., Seneviratne et al. 2010; Koster et al. 2015). Analysis of Eq. (10) shows that in regions with high climatological soil moisture ($\overline{m} \approx 1$), temperature anomalies are damped roughly twice as much as in regions where there is no soil moisture ($\overline{m} = 0$).

Using Eq. (10), the radiation-induced temperature variance in the absence of soil moisture anomalies is

$$\sigma^2(T_{\text{SW}}) = \frac{\sigma^2(F_{\text{SW}})}{(\alpha + L\nu\overline{m}\gamma)^2}. \tag{11}$$

Equation (10) also implies that the skewness in temperature variability driven solely by radiation anomalies is exactly equal to the skewness in observed shortwave radiation:

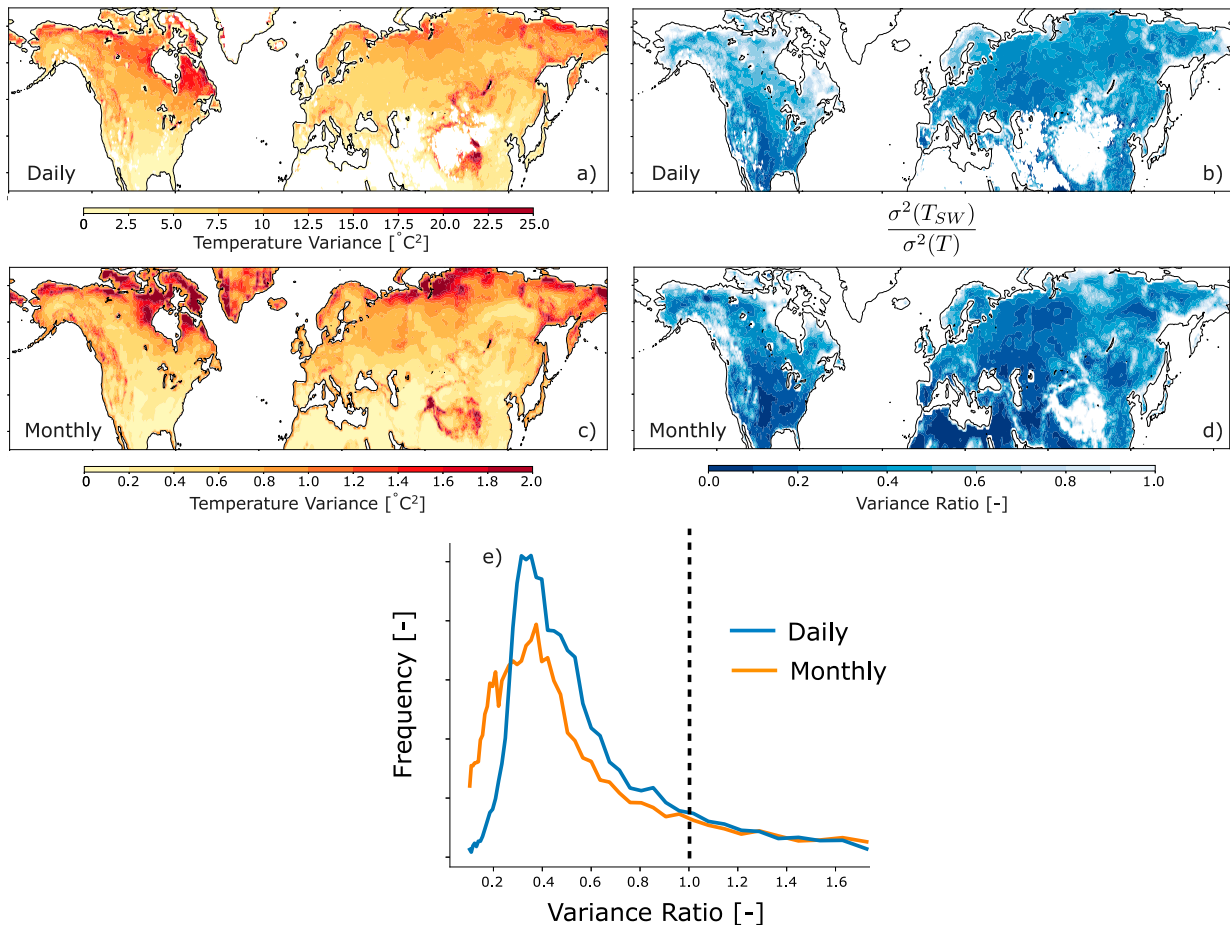$$S(T_{\text{SW}}) = S(F_{\text{SW}}). \tag{12}$$

FIG. 5. Radiation-induced temperature variance on (a) daily and (c) monthly time scales calculated using Eq. (11). (b),(d) The ratio of radiation-induced temperature variance on daily and monthly time scales to observed temperature variance from Figs. 2a and 2c, respectively. (e) The frequency distribution of the ratios mapped in (b) and (d). A value of one in (b), (d), or (e) indicated by the dashed black line in (e) implies that the temperature variance attributed to radiation variability in Eq. (11) perfectly matches the observations.

Substituting the observed daily and monthly absorbed shortwave radiation variance $\sigma^2(F_{SW})$ (Figs. 4a and 4c, respectively) into Eq. (11) yields the estimates of radiation-induced temperature variance on daily and monthly time scales (shown in Figs. 5a and 5c, respectively). Figures 5b and 5d show the ratio of the temperature variance obtained from Eq. (11) to the observed temperature variance on daily and monthly average time scales, and Fig. 5e shows the frequency distribution of these ratios across the extratropics. A value of 1 in Figs. 5b, 5d, and 5e implies that radiation-induced temperature variance from Eq. (11) is identical to the observed temperature variance. On average across the extratropics, our diagnostic model of radiation-induced temperature variability attributes 54% of the daily temperature variance to daily radiation variability, and 38% of the monthly temperature variance to monthly radiation variability.

In the absence of soil moisture anomalies, the SEMB simplifications derived above imply that skewness of temperature will be identical to the skewness in shortwave radiation on all time scales [Eq. (12)]. The spatial correlation between daily temperature and shortwave radiation skewness is $r = 0.49$ (Figs. 2b and 4b), but for monthly average data (Figs. 2d and 4d) the correlation between the two skewnesses is much weaker ($r = 0.09$). This is because a higher fraction of total temperature variance is attributable to shortwave radiation on daily time scales than on monthly time scales (54% vs 38%).

These modeling results highlight the important role of shortwave radiation variability in determining the shape of daily temperature probability distributions in the extratropics. On monthly time scales, our model attributes only one-third of the temperature variance to shortwave radiation variability and indicates that other mechanisms have primacy in driving temperature skewness.

b. Modeled radiation- and precipitation-induced temperature variability

To compare the impacts of shortwave radiation and precipitation variability on the statistical moments of summertime temperatures across averaging time scales, we return to our
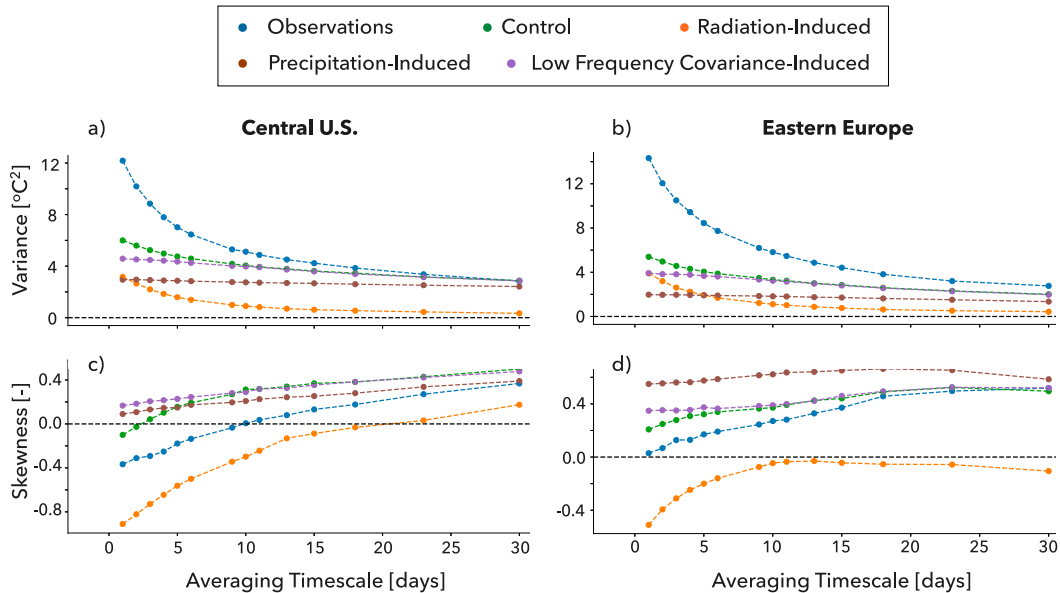
FIG. 6. As in Fig. 3, but adding results from three new experiments. The orange line shows results from the SEMB forced with the observed radiation forcing, but with soil moisture held constant at the summertime climatological value from the control simulations. The precipitation-induced and low-frequency covariance-induced experiments were forced by the same observed precipitation time series from the control simulations, but in the former, radiative forcing F_{SW} is held constant while in the latter it is filtered to remove variability in F_{SW} on time scales shorter than two weeks.

two case studies presented in section 2. Figure 6 shows results from the *control experiments* [i.e., Eqs. (7) and (8) forced by observed daily F_{SW} and P] shown in Fig. 3 along with three new experiments. In the *radiation-induced experiment* (orange dots/lines), soil moisture is held constant at the climatological value from the control simulations and the SEMB is forced only with the observed radiation time series for both regions; this is similar to our diagnostic radiation-induced temperature anomaly model [Eq. (10)]. In the *precipitation-induced experiment* (brown dots/lines), shortwave radiation is held constant at its climatological value and the temperature variability in the SEMB is induced entirely by precipitation. In the *low-frequency covariance-induced experiment* (purple dots/lines), the observed precipitation forcing is applied to the SEMB along with low-pass filtered shortwave radiation with a two-week cutoff time scale; temperature variability in this experiment includes the effects of covariance in the precipitation and low-frequency radiation forcings.

In both study regions, removing all soil moisture variability reduces daily average temperature variance compared to the control simulations (cf. the orange and green dots in Figs. 6a,b). The monthly average radiation-induced temperature variance is an extremely small fraction of the monthly average variance found in the control simulations. The radiation-induced temperature skewness is negative on daily time scales and tends toward zero as the averaging time scale increases in both regions considered. This is consistent with the expectations for an AR1 process from Proistosescu et al. (2016) and suggests that shortwave radiation acts as a randomly distributed forcing on the land surface. These results from the radiation-induced experiments are in line with our

more general findings presented in section 3a that (i) negative skewness in shortwave radiation contributes to the preponderance of negative skewness in observed daily temperature distributions across the extratropics (although soil moisture variability apparently damps the influence of this negatively skewed forcing in the SEMB control simulations) and (ii) monthly average radiation variability alone cannot account for skewness in monthly average temperature distributions.

In the precipitation-induced experiments in which shortwave radiation is held fixed (brown dots in Fig. 6), the simulated temperature variance and skewness decrease only slightly as averaging time scale increases, hinting at the important role of slowly varying soil moisture anomalies in the generation of low-frequency temperature variability. We will explore the implications of this result for low frequency temperature variability in the sections that follow. The precipitation-induced experiments also feature positive temperature skewness at all time scales, suggesting that as the averaging time scale increases, the increasingly positive temperature skewness seen in the observations in both study regions (blue lines in Figs. 6c,d) is driven by precipitation-induced temperature variability. The impact of precipitation forcing is clear even for daily variability. The temperature skewness seen in the radiation-induced experiments is much more negative than in the control experiments and in the observations (cf. the orange curves with the blue and green curves in Figs. 6c,d), demonstrating that precipitation-induced temperature variability in the SEMB reduces the effect of negatively skewed shortwave radiation forcing, even on daily time scales.

In the low-frequency covariance-induced experiments that include forcing due to precipitation and to low-frequency shortwave variability, daily average temperature variance is reduced compared to the control simulations (cf. the purple and green dots in Figs. 6a,b). However, on monthly time scales, the combination of precipitation and low-frequency radiation variability accounts for nearly all of the monthly average temperature variance found in the control experiments for both regions. Allowing low-frequency shortwave radiation variability to interact with precipitation forcing in the SEMB increases the positive monthly temperature skewness over the central United States relative to the precipitation-induced experiments (cf. the brown and purple dots in Fig. 6c). In eastern Europe however, the temperature skewness driven by precipitation alone is larger than the temperature skewness induced by the covariance between low-frequency shortwave radiation and precipitation. In separate SEMB experiments forced by low-pass filtered radiation and with fixed soil moisture (not shown) we found that the monthly averaged SEMB temperature output is negatively skewed in eastern Europe and slightly positively skewed in the central United States. This explains the contrasting skewness results in the covariance experiments in these regions but does not change the fact that precipitation-induced temperature variability acting alone or combined with low-frequency radiation variability creates positively skewed temperature distributions in the SEMB simulations of both study regions.

Collectively, the SEMB experiments suggest that the variance in long-lived (e.g., monthly average) summertime temperature anomalies in the central United States and eastern Europe is induced primarily by precipitation and by the covariance of precipitation and low-frequency solar radiation variability [see also Vargas Zeppetello et al. (2020a) for an analysis that encompasses the entire extratropics]. Results from the SEMB and the diagnostic equation for radiation-induced temperature variance [Eq. (11)] suggest that observed positive skewness in low-frequency temperature anomalies in both of these regions is driven by precipitation variability; it cannot be explained by radiation forcing alone. In the next two sections, we develop an analytical model that illuminates the processes by which soil moisture variability impacts temperature variability, and ascertain the primacy of these processes for driving low-frequency temperature variability and the clustering of extremely hot days throughout the extratropics.

4. Soil moisture variability and positive temperature skewness

Many studies have noted that soil moisture, because of its relationship to evapotranspiration and the surface energy budget, is a crucial driver of temperature variability during summertime (e.g., Delworth and Manabe 1988; Seneviratne et al. 2010). In this section, we modify the SEMB equations to explore how soil moisture variability impacts the probability distribution of summertime temperature when the land surface energy budget is in steady state (relative to the soil moisture budget). We begin by fixing insolation at its climatological

average value and neglecting the time tendency term in Eq. (7). The resulting equation eliminates shortwave radiation variability as a forcing:

$$0 = \overline{F_{SW}} - \alpha(T - T_D) - L\nu_L m[q_s(T) - \overline{q}]. \tag{13}$$

Equation (13) specifies the relationship between m and T for constant $\overline{F_{SW}}$ and $\overline{q}$. The set of all T and m values that satisfy Eq. (13) for a particular set of parameters (r_s, $\overline{q}$, $\overline{F_{SW}}$, etc...) is a "steady-state set"—a curve in temperature–soil moisture phase space that is relevant to low-frequency variability, that is, on time scales longer than the equilibration time scale of the surface energy budget (1–2 days).

To see how these steady-state sets can be used to understand the shape of the temperature distribution, Fig. 7a shows a hypothetical linear steady-state set with a dashed line. In this case, the temperature distribution would be an exact reflection of the soil moisture distribution; positively skewed soil moisture distributions (characteristic of dry regions in ERA5) would lead to positively skewed temperature distributions and vice versa for negatively skewed soil moisture distributions (characteristic of wet regions). In contrast, the solid curve in Fig. 7a shows the steady-state set generated by substituting realistic values of climatological atmospheric specific humidity $\overline{q}$, shortwave radiation $\overline{F_{SW}}$, and surface resistance r_s into Eq. (13). The important aspect of this physically based steady-state set is that a given negative soil moisture anomaly $-\delta m$ results in a temperature anomaly much greater in magnitude than one that results from a positive soil moisture anomaly of the same magnitude $+\delta m$. Hence, a Gaussian soil moisture distribution (skewness = 0) results in a positive temperature skewness, although positively skewed soil moisture distributions could still result in negative temperature skewness and will be examined below. The source of the nonlinear behavior evident in the steady-state set in Fig. 7a is the feedback between soil moisture, evaporative cooling, and atmospheric water vapor demand (Vargas Zeppetello et al. 2019): since the vapor pressure deficit is larger in a dry climate (low $\overline{m}$) than in a wet climate, a fluctuation in soil moisture in a dry climate causes a greater evaporation perturbation and thus a greater impact on the surface energy budget than in a wet climate (high $\overline{m}$). This feedback sets an effective cap on surface cooling via evapotranspiration that is evident from the shape of the solid curve in Fig. 7a.

The sensitivity of the steady-state sets defined by Eq. (13) to the climatological specific humidity $\overline{q}$, shortwave forcing $\overline{F_{SW}}$, and resistance parameter r_s is shown in Figs. 7b–d, respectively. All realistic parameter combinations feature the nonlinear dependence of temperature on soil moisture that would render a positively skewed temperature distribution if the distribution of soil moisture anomalies were Gaussian (i.e., nonskewed). Since the nonlinearity of the steady-state sets is tied to the feedback between temperature, evaporation, and soil moisture, any changing climatological parameter that reduces the climatological (mean state) evaporation will lead to a more linear steady-state set while any environmental modifications that increase climatological evapotranspiration will accentuate the nonlinearity of the steady-state sets.
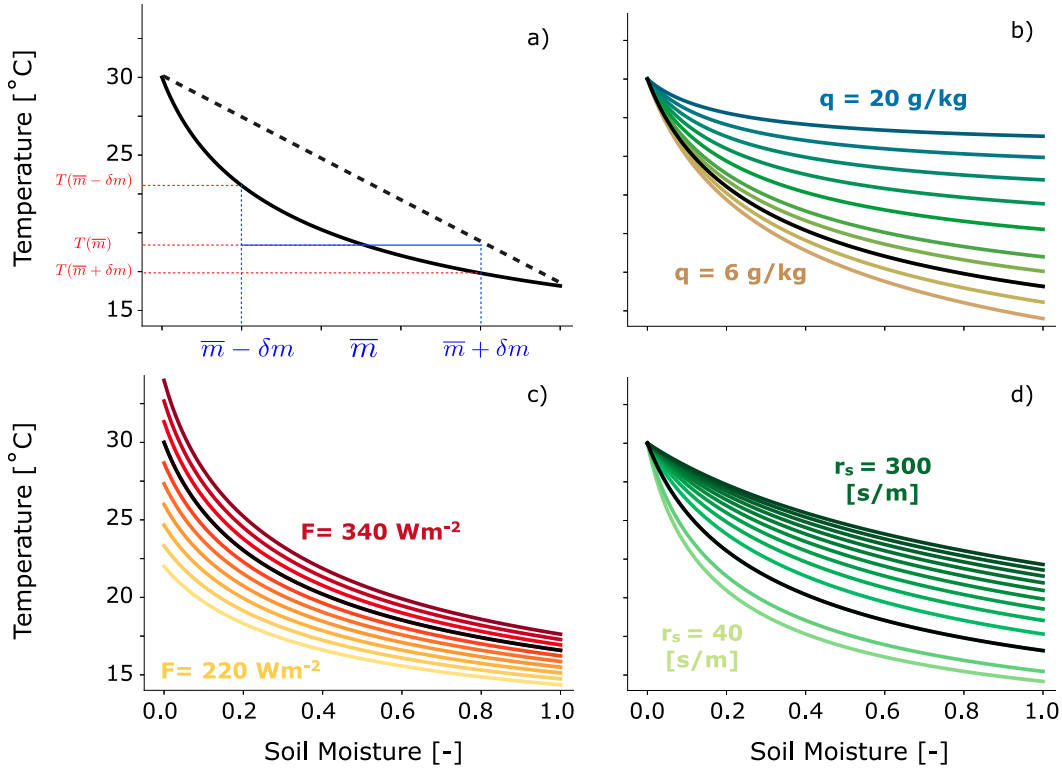
FIG. 7. Steady-state sets in temperature–soil moisture phase space for various land surface and climate parameters. (a) A physically constrained steady-state set using Eq. (13) with average parameter values of shortwave radiation, specific humidity, and surface resistance (solid line), and another hypothetical, linear steady-state set (dashed line) for conceptual purposes. (b)–(d) Steady-state sets computed using Eq. (13) with various values of climatological specific humidity, net shortwave radiation, and surface resistance, respectively. The curve shown in (a) using the nominal parameters is reproduced in black in (b)–(d).

We can quantify the impact of the underlying soil moisture probability density function on temperature variability by further simplifying Eq. (13). A Taylor expansion of the equation for vapor pressure deficit about the dewpoint temperature T_D gives

$$q_s(T) - \overline{q} = q_s(T_D) - \overline{q} + \frac{dq_s}{dT}(T - T_D) \equiv \gamma(T - T_D),$$
(14)

where $q_s(T_D) - \overline{q} \equiv 0$ by definition and, as in Eq. (9), $\gamma \equiv dq_s/dT$. Inserting Eq. (14) into Eq. (13), we obtain

$$0 = \overline{F_{SW}} - \alpha(T - T_D) - L\nu_L m\gamma(T - T_D) \text{ or} \quad (15)$$

$$T - T_D = \frac{\overline{F_{SW}}}{\alpha + L\nu_L \gamma m}.$$
(16)

The differences between steady-state sets calculated according to Eqs. (13) and (16) are small (not shown). We can use Eq. (16) to describe temperature anomalies associated with moisture fluctuations that last longer than the equilibration time for the surface energy budget—a day or two. Given a probability density function for soil moisture $g(m)$, the temperature probability density $f(T)$ is (see Papoulis 1965):

$$f(T - T_D) = g(m)\left|\frac{dT}{dm}\right|^{-1}.$$
(17)

Combining the steady-state set shown in Fig. 8a with two idealized $g(m)$ PDFs (shown in Fig. 8b), we obtain the temperature PDFs $f(T - T_D)$ shown in Fig. 8c. One soil moisture density function is normally distributed (blue; zero skew), qualitatively consistent with the monthly soil moisture distribution for a humid location (the central United States); the other is a gamma distribution (brown; positive skew), qualitatively consistent with that for an arid climate (the western United States). While both soil moisture distributions cause positively skewed temperature density functions; temperature skewness is greater for the Gaussian soil moisture distribution.

Collectively, the results of sections 2c and 3b show that positive skewness in observed monthly average temperature variability can be induced by precipitation alone, in agreement with analyses of global climate models in fixed soil moisture experiments (Berg et al. 2014). In this section, we have shown that stochastic, low-frequency variations in soil moisture generate temperature distributions that are positively skewed because of the intrinsic nonlinear relationship between temperature, soil moisture, and evapotranspiration.
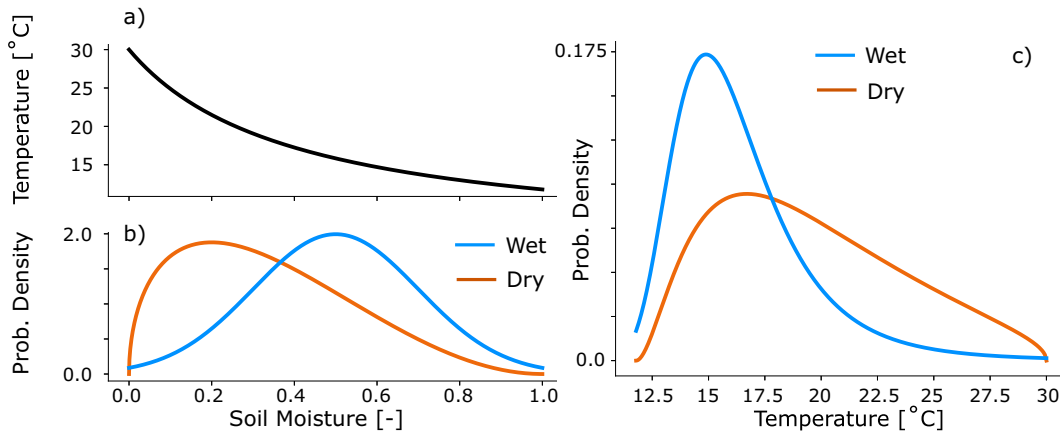
FIG. 8. (a) A steady-state set generated by applying average parameter values to Eq. (16). (b) Two hypothetical soil moisture probability density functions chosen to emulate soil moisture distributions of dry and wet regions in the ERA5 reanalysis. (c) Temperature probability density functions calculated according to Eq. (17) from the steady-state set shown in (a) and each soil moisture density function shown in (b). In (c), temperature on the x axis is offset from the dewpoint temperature T_D.

5. A random precipitation model of summertime soil moisture variability

Soil moisture is generated by precipitation events that, to first order, are randomly distributed in time (Eagleson 1978). In this section, we develop the *random precipitation model* for summertime soil moisture that is driven by random precipitation impulses and, when combined with the surface energy budget [Eq. (7)], agrees qualitatively with the essential patterns of observed monthly average temperature skewness across the extratropics.

Soil moisture is replenished by precipitation events and depleted over "inter-storm" periods (McColl et al. 2019). Eagleson (1978) demonstrated that precipitation can be well modeled as an event-based Poisson process with average event frequency ω and intensities given by a gamma distribution; we will refer to these time series as "random precipitation forcing." Building on his results, we run the SEMB for one summer (92 days) with random precipitation forcing and constant shortwave radiation $\overline{F_{\mathrm{SW}}}$. Figure 9 shows the results from the in temperature–soil moisture phase space (gray line). Four precipitation events occurred in this 92-day simulation. In Fig. 9a we have added arrows that indicate the temporal evolution of the state variables (T, m) through phase space and added purple circles to denote 24-h increments in the continuum shown by the dashed gray line.

Figure 9b shows a schematic of the important, generic pattern found in the experiment described above. The period immediately following an instantaneous precipitation event (blue arrows in Fig. 9b) is characterized by a decrease in temperature because more soil moisture is available for enhanced evapotranspiration (green arrows). The surface heat capacity is small, so the cooling occurs rapidly; we refer to this short period as the "storm moisture cooling." Following this rapid cooling, a slow drying by evapotranspiration occurs and the land surface (slowly) warms in a manner that nearly follows the steady-state set derived in section 4, which is shown with a

thick black line in Fig. 9a. The warming and drying trajectory followed by the SEMB simulation (gray lines and purple circles) is nearly coincident to the steady-state set. The close spacing of the 24-h increments (purple circles in Fig. 9a) in the warming and drying phase of the simulation occurs because the drying time scale of the land surface is much longer than the cooling time scale immediately following a precipitation event.

a. Deriving the random precipitation model of summertime soil moisture

The results of the SEMB experiment shown in Fig. 9a motivate an even simpler model of soil moisture. By treating precipitation events as instantaneous spikes of variable magnitude p_n, we can write a simplified version of the surface moisture budget [Eq. (8)] that neglects the coupling between anomalies in evaporation and temperature:

$$\mu \frac{dm}{dt} = \frac{dJ}{dt} - \nu_L m \overline{V}, \tag{18}$$

where μ and ν_L are defined in section 2, $\overline{V}$ is the climatological average vapor pressure deficit, and

$$J = p_1 + p_2 + \cdots + p_N \tag{19}$$

represents a Poisson series of precipitation events with average frequency ω. This model of soil moisture assumes a fixed value of potential evapotranspiration given by $\nu_L \overline{V}$. A similar version of Eq. (18) was developed to explain simulated soil moisture in an early climate model (Delworth and Manabe 1988), but our consideration of precipitation as events with a Poisson distribution rather than a continuous white noise time series is more realistic. An idealized model of a similar precipitation-induced phenomena (cloud aerosol sinks) is found in Baker et al. (1979). The solution to Eq. (18) subject to the forcing J given by Eq. (19) is a sum of exponential decays
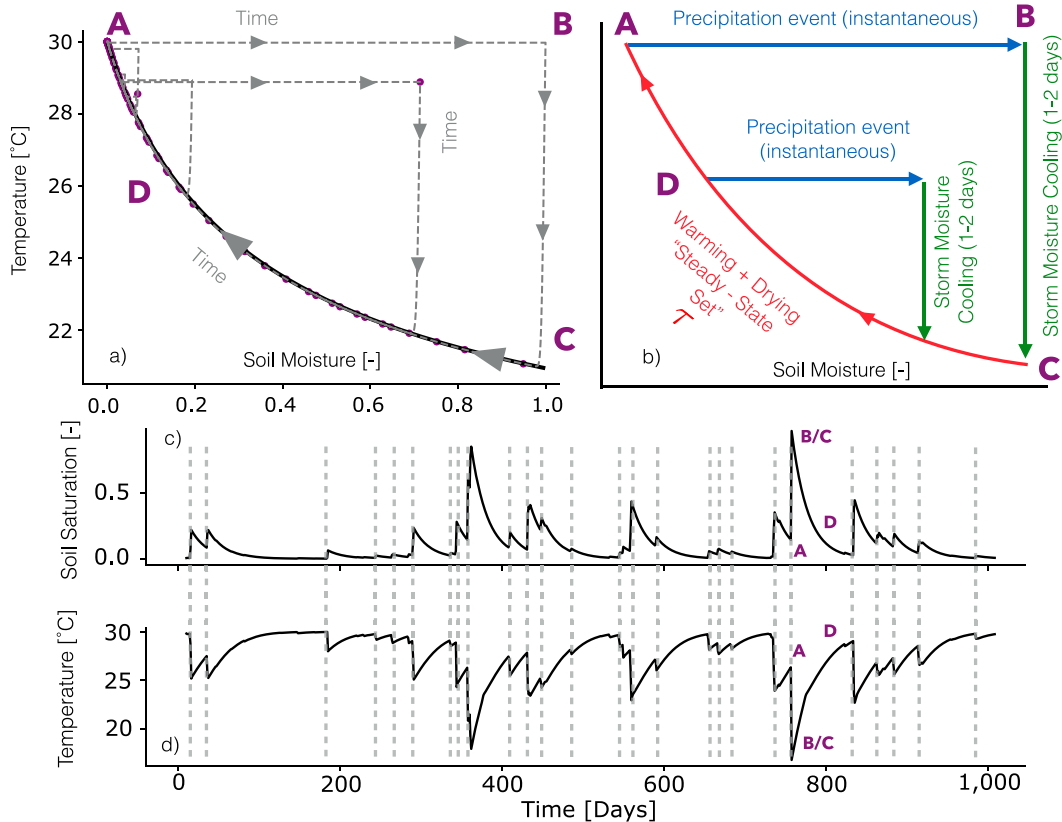
FIG. 9. (a) The gray line shows output from the SEMB as a trajectory through soil moisture–temperature phase space from an experiment that used constant shortwave radiation forcing and random precipitation forcing. The black line shows the steady-state set calculated from the model parameters used in this simulation. Purple circles show the 24-h increments of the 92-day simulation; gray arrows indicate the temporal evolution of the state variables T and m. (b) A schematic of this evolution, decomposed into three stages: an instantaneous precipitation event, a rapid storm moisture cooling, and a longer interstorm warming and drying period. (c) A solution (soil moisture) of the random precipitation model [Eqs. (18)–(21)]; (d) the temperature time series that results from using the soil moisture from (c) as a forcing for the surface energy budget [Eq. (7)]. Vertical gray lines in (c) and (d) indicate the timing of precipitation events. Purple letters in all panels describe the stages of a land surface trajectory in the absence of variability in radiation forcing; the random precipitation model treats the precipitation event and the post storm cooling as instantaneous, hence the combination of stages B/C in (c) and (d).

$$m(t) = \sum_{n=0}^{N} p_n \exp[-(t - t_n)/\tau], \qquad (20)$$

where $t \geq t_n$ and N is the total number of precipitation events p_n that occur at time t_n, and

$$\tau \equiv \frac{\mu}{\nu_L \overline{V}}. \qquad (21)$$

Equations (18)–(21) comprise the *random precipitation model*. Equation (20) says that the moisture at time t is equal to the sum of the residual moisture from past precipitation events that has not yet been lost to evapotranspiration. Here τ is the characteristic *e*-folding time scale on which the land surface dries by evapotranspiration in the absence of precipitation. The soil moisture time series output from our random precipitation model is an example of "shot noise" (see Papoulis 1965). By using soil moisture output from the

random precipitation model [Eq. (20)] as a forcing on the surface energy budget [Eq. (7)] and neglecting fluctuations in shortwave radiation, we obtain the *random precipitation model of summertime temperature variability*.

There are two important distinctions between the governing equations for soil moisture in the random precipitation model and the SEMB. First, changes in temperature do not impact soil moisture in Eq. (18); the evapotranspiration rate is a function of the climatological vapor pressure deficit $\overline{V}$ and the invariant surface resistance r_s. Hence, under cooler conditions than climatology, the drying in the random precipitation model will be faster than in the full SEMB and in reality (and vice versa: under warmer conditions, drying will be slower in the random precipitation model than in the SEMB) because the evapotranspiration rate is not affected by surface temperature anomalies. Second, the random precipitation model has no cap on soil moisture, whereas in the SEMB, runoff and

infiltration fluxes act to constrain m to a value between zero and one.

An example solution to the random precipitation model is shown in Fig. 9c; it is generated from Eq. (20) with random precipitation forcing with an average precipitation frequency of one event every five days. Substituting the resulting soil moisture output from the random precipitation model (Fig. 9c) into the surface energy budget with fixed shortwave radiation, we obtain the temperature time series shown in Fig. 9d. The purple letters in Figs. 9c and 9d roughly correspond to the stages that we identified in the SEMB experiment shown in Figs. 9a and 9b.

b. Moments of soil moisture in the random precipitation model

The moments of the soil moisture distribution in the random precipitation model [Eq. (18)] can be calculated analytically and expressed simply in terms of a nondimensional number

$$Z \equiv \omega\tau, \tag{22}$$

where, as in Eq. (20), τ is the characteristic time scale of land surface drying through evapotranspiration [Eq. (21)] and ω is the average event frequency of precipitation. The appendix details the calculations of the moments of m. For precipitation event intensities p_n given by a gamma distribution with average event intensity p_o, the first three moments of soil moisture are

$$\overline{m} = p_o Z, \tag{23}$$

$$\sigma^2(m) = \left(p_o^2 + p_o\right)Z, \text{ and} \tag{24}$$

$$S(m) = \frac{2p_o + 3p_o^2 + p_o^3}{\left(p_o^2 + p_o\right)^{3/2}} \frac{2^{3/2}}{3\sqrt{Z}}. \tag{25}$$

The moments of temperature in the random precipitation model of temperature variability cannot be calculated analytically; they must be calculated from simulations where soil moisture output from the random precipitation model is used as a forcing on the surface energy budget [Eq. (7)]. In the following section, we discuss experiments that compare output from the random precipitation model of temperature variability to the SEMB.

6. The Z parameter explains summertime soil moisture and temperature variability

To compare the SEMB to the random precipitation model of temperature variability, we simulate a range of climates using both. To do this, 20 pairs of specific humidity $\overline{q}$ and average precipitation frequency ω were applied to both models to simulate climates that range from extremely arid (low $\overline{q}$ and ω) to extremely humid (high $\overline{q}$ and ω). While the potential combinations of $\overline{q}$ and ω are endless, we found that observed ω and climatological $\overline{q}$ from ERA5 are correlated,

effectively eliminating some combinations of $\overline{q}$ and ω from consideration. For example, it is extremely unlikely for a region with high precipitation frequency to also have extremely low $\overline{q}$; this feature of continental climates helped guide our selection of the parameter pairings. In all simulations, the intensities of precipitation impulses were drawn from a gamma distribution; all model parameters, including the event average precipitation and climatological shortwave radiation, come from the eastern European star in Fig. 2 and are detailed in Table 1. For each $(\overline{q},\omega)$ pair, an ensemble of 1000 simulations is performed with the SEMB and the random precipitation model—both driven by random precipitation forcing and constant F_{SW}. Each simulation is for 1000 days, and the last 500 days are used to calculate moments of temperature and soil moisture for each simulation then averaged across all 1000 simulations. To calculate τ and Z, we need the climatological vapor pressure deficit, which is calculated using the mean temperature simulated by the respective model. For the random precipitation model, this introduces a slight inconsistency because an a priori mean temperature was used in the calculation of $\overline{V}$ [see Eq. (18)] that was subsequently used in Eq. (21) to obtain the a posteriori τ.

Figure 10 shows the first three statistical moments (mean, variance, and skewness) of daily average soil moisture and temperature as a function of the climatological Z parameter from each of the twenty background climate simulations. While we present moments of daily average data, the moments are fairly insensitive to averaging time scale (similar to the results from precipitation-induced experiments presented in Fig. 6). Because the analytical expression for the soil moisture moments is continuous in Z [Eqs. (23)–(25)]; these solutions are plotted as dashed black lines in Figs. 10a–c. All other moments are calculated from either the SEMB simulations (blue dots), or from using the time series generated by the random precipitation model as a forcing on Eq. (7) (black dots in Figs. 10d–f).

a. Soil moisture moments in the SEMB and random precipitation model

Figures 10a–c show that the moments of soil moisture from the SEMB are in qualitative agreement with those from the random precipitation model. The differences between the two models illuminate the impact of temperature anomalies on evapotranspiration and the physical limits imposed on soil moisture by runoff and infiltration in the SEMB that are not included in the random precipitation model. The mean soil moisture in the random precipitation model is a linear function of Z, reflecting both the increase in average precipitation frequency ω and decrease in evaporative demand by increasing $\overline{q}$. The increase in $\overline{m}$ with Z is sublinear in the SEMB experiments (Fig. 10a), likely because of the physical cap on soil moisture in the SEMB that does not permit unphysically high values of soil moisture ($m > 1$) to contribute to $\overline{m}$.

The variance in soil moisture differs significantly between the SEMB and the random precipitation model (Fig. 10b). The random precipitation model features a linear relationship between Z and $\sigma^2(m)$ [Eq. (24)], but the SEMB experiments
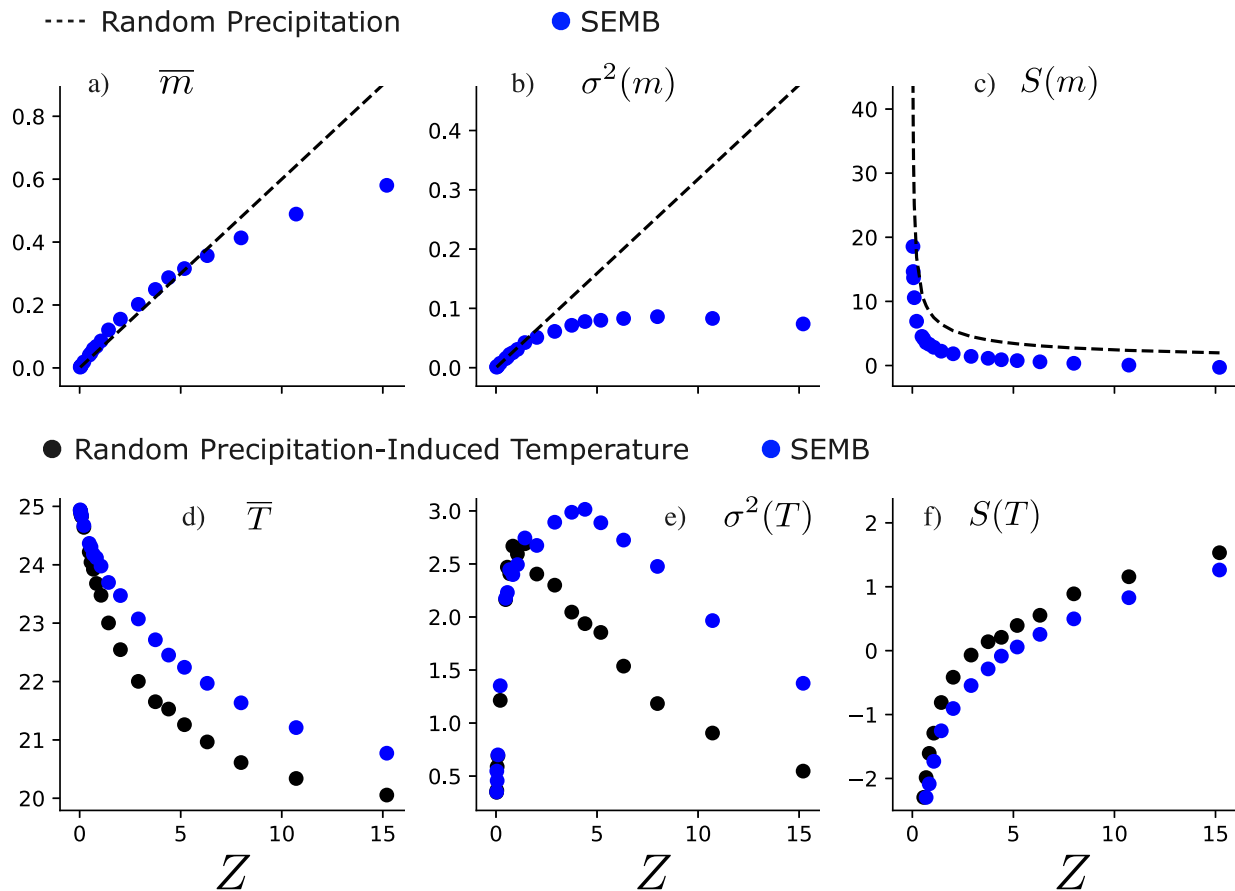
FIG. 10. The first three moments of (a)–(c) soil moisture and (d)–(f) temperature from the fully coupled SEMB (blue dots), and from the random precipitation model (black lines and dots) for the same set of 20 different $\overline{q}$ and ω pairs. The moments of soil moisture in the random precipitation model are known analytically [Eqs. (23)–(25)] and hence shown as a continuous black line.

show a saturation of $\sigma^2(m)$ for $Z > 5$. This is likely due to both the lack of a soil moisture constraint in the random precipitation model that allows extreme precipitation events to overfill the soil moisture bucket, and to the negative feedback between soil moisture, evaporative cooling, and vapor pressure deficit that suppresses evapotranspiration anomalies at high values of soil moisture in the SEMB but not in the random precipitation model.

Despite the differences in the variance, the SEMB and the random precipitation model broadly agree in the relationship between soil moisture skewness and Z (Fig. 10c). For low values of Z, both models feature very large positive skewness associated with extremely infrequent precipitation events that induce large positive soil moisture anomalies. As the average frequency of precipitation events increases, the skewness tends toward zero in both the SEMB and the random precipitation model. In the SEMB, the skewness dips below zero for high Z values because the cap on soil moisture prevents a long tail from developing on the wet side of the soil moisture distribution. This result aligns with soil moisture output from the ERA5 reanalysis, which also shows a transition from

positive skewness in dry regions to negative skewness in wet regions (not shown).

b. Temperature moments in the SEMB and the random precipitation model

Figures 10d–f show qualitative agreement between the SEMB and the random precipitation model of temperature variability in the first three moments of the temperature distribution. The mean temperature in the random precipitation model is cooler than that in the SEMB for high Z values, consistent with the higher mean soil moisture values in the random precipitation model (Fig. 10d). However, both models exhibit the same nonlinear relationship between Z and $\overline{T}$ that was seen in Fig. 7 [this is expected because $\overline{T} \propto \overline{m}^{-1}$ in Eq. (16) and $\overline{m} \propto Z$ in Eq. (23)].

Both models show very low variance for small values of Z (Fig. 10e). As Z increases, temperature variance quickly increases. At intermediate Z values, the mean temperature (and therefore vapor pressure deficit) is still relatively high, meaning that soil moisture anomalies generate large evaporative cooling anomalies that increase the temperature variance.

As Z continues to increase, the coupling between evaporation and vapor pressure deficit reduces the impact of soil moisture anomalies on evapotranspiration, thereby reducing the temperature variance (see Seneviratne et al. 2010; Vargas Zeppetello et al. 2019).

Finally, the temperature distributions from both models feature a transition from negative skewness to positive skewness as Z increases. Without variability in shortwave radiation, infrequent precipitation events in otherwise arid climates (low Z) tend to produce extremely cold temperatures, and hence negative temperature skewness. As Z increases, the background climate becomes more humid and the temperature becomes positively skewed because infrequent dry spells become the dominant driver of extremely warm temperatures.

The results from the random precipitation model of temperature variability have profound implications for the emergence of heat waves. In this simple model of precipitation-induced temperature variability, extreme and persistent warm periods are the result of infrequent, long-lived dry spells in otherwise humid climates. In both models, long-lived heat waves emerge naturally in relatively humid climates because of the nonlinear relationship between evapotranspiration, soil moisture, and temperature that ensures that relatively infrequent dry spells generate disproportionately high temperatures compared to wet spells. Next, we will discuss the implication of these results for understanding observed temperature statistics on daily and monthly time scales, and the clustering of extremely hot days in the hottest months.

c. Monthly average temperature skewness across the extratropics

Using climatological temperature and precipitation from observations and specific humidity from ERA5, we calculate τ, ω, and Z across the extratropics. Maps of these three values are shown in Fig. 11. Figure 12 shows the relationships between climatological Z and the monthly average temperature skewness over the extratropics, within Europe (the red box in Fig. 11c) and within the United States (red contour in Fig. 11c). The 2D histograms (gray lines) are constructed by counting all the grid cells that fall into each bin increment of size δZ, $\delta S(T)$, and then dividing by the total number of grid boxes in the domain of interest. Figures 12b, 12d, and 12f show cumulative distribution functions of positive and negative skewness as a function of Z for grid boxes where the monthly average temperature skewness is statistically distinguishable from zero (see Fig. 2d).

Across the extratropics, monthly average temperature skewness is at its lowest average value at $Z \sim 0$ and increases from there roughly linearly until $Z \sim 2$, above which it stays roughly constant. This distribution is in qualitative agreement with results from the SEMB and the random precipitation model of temperature variability shown in Fig. 10f, where the lowest skewness values are at $Z \sim 0$ and increase as Z increases. Higher-order moments such as skewness are sensitive to the data quality, to complement the results across the extratropics, we show the pattern of skewness as a function of
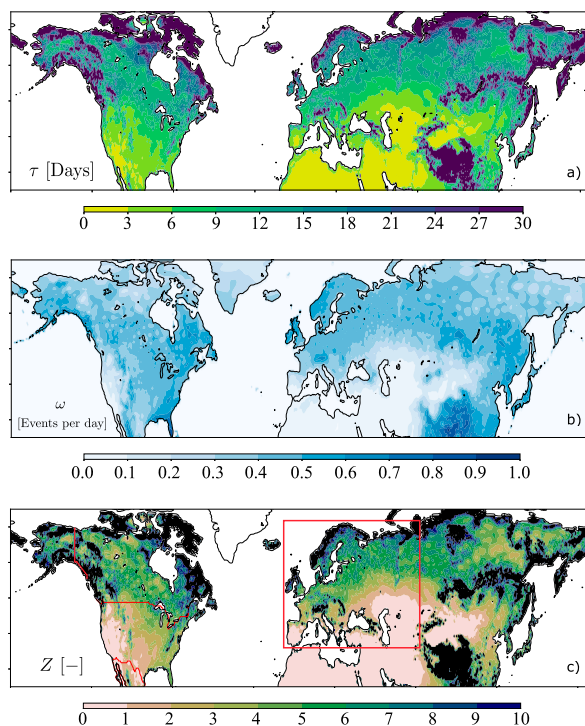

FIG. 11. (a) τ, the time scale of soil moisture depletion calculated according to Eq. (21) using climatological mean summertime temperature from Willmott and Matsuura (2018) and near-surface specific humidity from ERA5. (b) Average frequency of precipitation derived from the CPC daily precipitation data. (c) The nondimensional Z parameter, obtained by multiplying the top two panels. The red box and contours indicate the study regions for the analysis presented in section 6c.

Z over only Europe and the United States (Figs. 12c and 12e, respectively), as these are the regions that are least likely to suffer from the smoothing of a low-density network of observations. The cumulative distributions in Figs. 12b, 12d, and 12f show the distinct clustering of positive and negative monthly average temperature skewness. Negative skewness is more highly concentrated toward low Z values, in agreement with the random precipitation model, while positive temperature skewness is more equally distributed over the Z spectrum. The distinct clustering of monthly average temperature skewness is particularly evident in Europe, where 98% of the grid boxes with negatively skewed monthly average temperature distributions have $Z < 2$ and 93% of grid boxes with positively skewed monthly average temperature distributions have $Z > 2$ (see Fig. 12d). Over the United States 71% of the negatively skewed monthly average temperature distributions lie in grid boxes with $Z < 1$ and 80% of the grid boxes with positive skewness have $Z > 1$ (see Fig. 12f).

The random precipitation model of temperature variability captures the basic relationship between monthly average temperature skewness and climatological Z in the observations throughout the extratropics, but there is considerable spread in the observations. We expect this spread is due to spatial
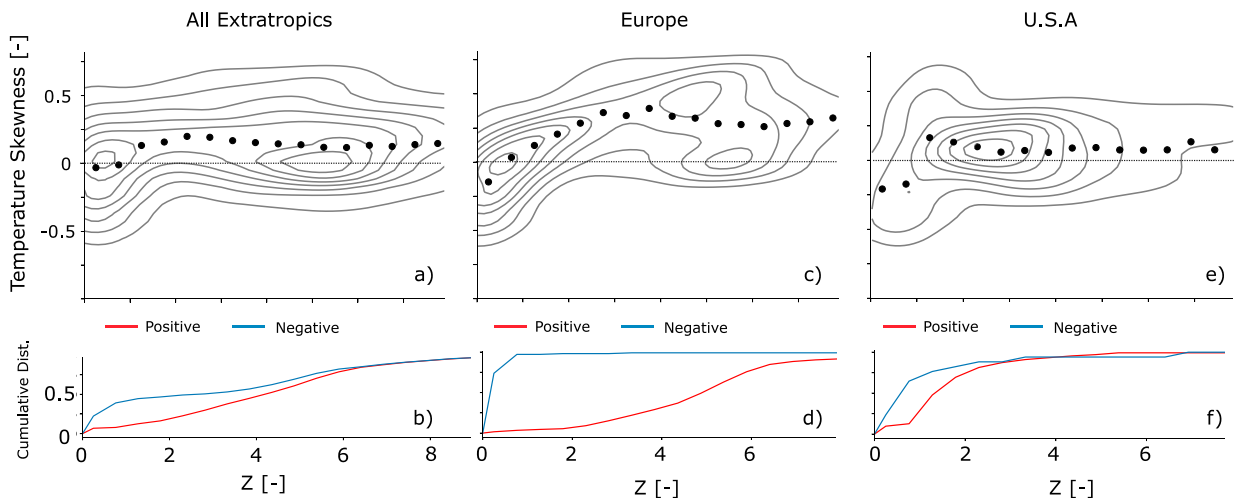
FIG. 12. (a) 2D histograms of the observed monthly average temperature skewness plotted against climatological Z (Fig. 11c); black dots show the averages over all grid boxes within evenly spaced Z bins of width 0.5. (b) Cumulative distributions of positive (red) and negative (blue) skewness values as a function of climatological Z in the extratropics. Only grid boxes where the monthly average temperature skewness is statistically distinguishable from zero are shown in the cumulative distributions (see contours in Fig. 2d). (c),(d) As in (a) and (b) but over Europe; (e),(f) as in (a) and (b), but over the United States.

variations in r_s and μ that we do not consider in our calculation of climatological Z as well as from other assumptions within our model. These regional variations in r_s and μ are due to regional differences in plant physiology, root structure, and soil properties. Also note that as $Z \rightarrow 0$ in extremely dry regions, the temperature variance driven by precipitation also decreases (Fig. 10e) and the variance in temperature is primarily due to shortwave radiation forcing. Hence, as $Z \rightarrow 0$, skewness approaches that of the shortwave forcing, typically -0.1 ± 0.3 (see Fig. 4d), rather than the extremely low values projected by the random precipitation forcing (Fig. 10f).

7. Meteorological droughts and extremely hot days

In the sections above, we have used simple models to illuminate the processes that give rise to positively skewed temperature variability on monthly time scales. Months in the long, warm tail of the random precipitation-induced temperature variability distributions are the very heat waves during which there is an inordinately large number of extremely hot days throughout the extratropics (see Fig. 1). As concrete examples, we show in Fig. 13 the summertime temperature anomalies (the seasonal cycle has been removed; see section 2a) and daily precipitation over Dallas, Texas ($Z \sim 2$), and Moscow, Russia ($Z \sim 6$), for the two summers in each city that had the greatest number of days during which the 95th temperature percentile was exceeded in the years 1985–2014: the summers of 1999 and 2010 in Russia and the summers of 1996 and 2011 in Texas (see Miralles et al. 2014; Fernando et al. 2016). Days with the highest temperatures occur during periods of extended meteorological drought. The summer of 2011 in Dallas (Fig. 13a) is the best example of this behavior; there were only four above-average precipitation events in the entire summer, while 37 days

registered temperature anomalies that were above the local 95th percentile for that location over a 30-yr period (representing more than one-quarter of the total local 95th temperature percentile exceedances). A similar situation prevailed for June and July of 1996 in Dallas, for the end of June through the beginning of August of 2010 in Moscow, and for June of 1999 in Moscow.

While not all dry spells lead to heat waves, and nonlocal effects have been shown to contribute to extremely high daily temperatures (Miralles et al. 2014; Linz et al. 2018; Tamarin-Brodsky et al. 2020), our results demonstrate that extremely hot monthly average temperatures are expected due to relatively infrequent meteorological droughts in regions where Z, the product of average precipitation frequency (ω) and the soil moisture drying time scale (τ), is moderate or high. Figure 13e shows the percentage of cumulative summertime rainfall over a 30-yr period (1985–2014) that fell during the three hottest months of the historical record; if rainfall and temperature were completely independent from one another, this value would be 3% everywhere (shown in the green contour). Across the extratropics, we see reduced rainfall in connection with the hottest months of the historical record. Across the extratropics, 1% of total 1985–2014 JJA precipitation fell during the three hottest months on average. Combined with the inordinate number of extremely hot days during the hottest months (Fig. 1a) these findings suggest that meteorological drought is the primary forcing agent of extremely hot months across the extratropics, as predicted by the random precipitation model. These results provide observational evidence for our conclusion that across the extratropics long-lived extremely high temperatures (i.e., heat waves) are due to infrequent extended dry spells. These are the very heat waves during which there is an inordinately large
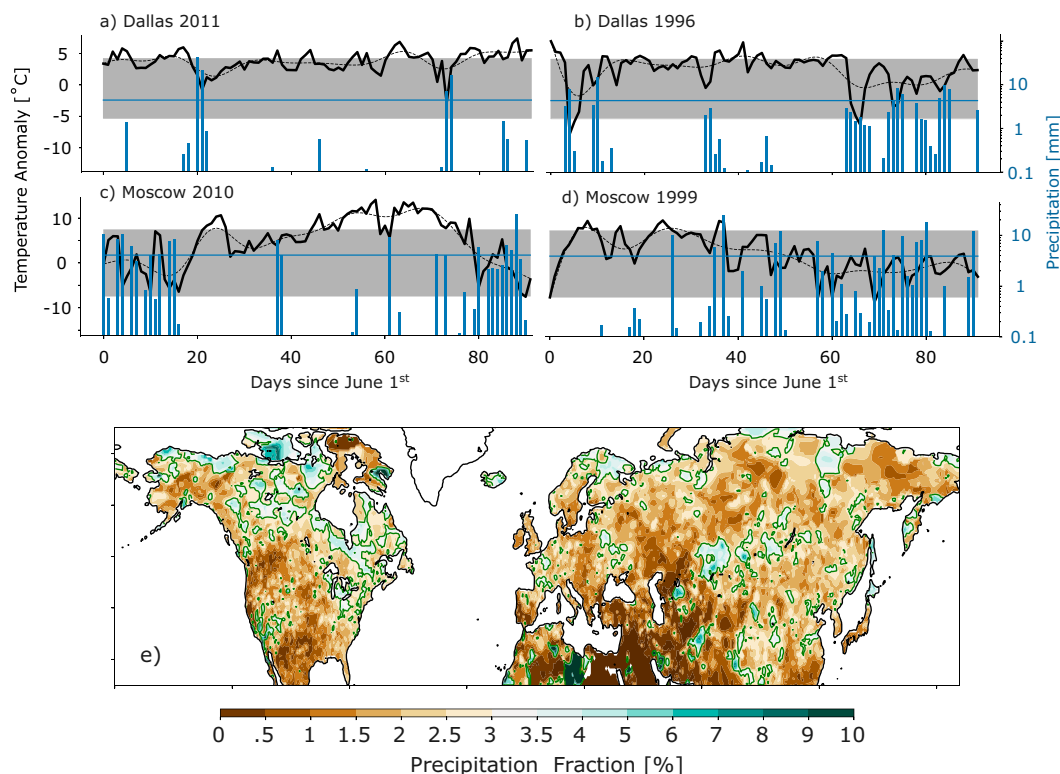
FIG. 13. Two summers of daily maximum temperature anomalies (thick black lines) and precipitation (blue bars; log scale) in (a),(b) Dallas and (c),(d) Moscow. Dashed black lines show the low-pass filtered temperature time series with a two-week cutoff time scale; gray shading shows the 5th–95th percentile range for the 1985–2015 period. The horizontal blue line shows the event average daily precipitation for the 30-yr period. (e) Percentage of cumulative JJA rainfall that fell during the three hottest months from 1985–2014; green line shows the 3% value that we would obtain if precipitation and temperature were completely unrelated.

number of extremely hot days throughout the extratropics (see Fig. 1).

8. Conclusions

We began this study by documenting the number of extremely high daily temperatures recorded in the three hottest months of the historical record and the moments of summertime daily and monthly temperature distributions. Over most of the extratropics, the number of extremely hot days in the three hottest months of the historical record (N_e) is 50% greater than expected from simple statistical models. We also show that temperature skewness either changes from negative on daily time scales to positive on monthly time scales or shifts to a greater positive value at longer time scales over more than half of the land area in the extratropics, both of which are in stark contrast with the central limit theorem's prediction for a simple AR1 process driven by a (negatively) skewed daily forcing, implying that the processes that govern temperature variability are time scale dependent. In this study, we develop a model of the surface energy and moisture budgets (the SEMB) that, when forced by the observed net absorbed shortwave radiation and precipitation, reproduces the observed shift from

negative to positive skewness as the averaging time scale is increased from one day to one month in two case study regions (the central United States and eastern Europe).

We perform a series of experiments with the SEMB that confirm that shortwave radiation variability is a principal driver of variance and skewness of *daily* summertime temperatures. Without soil moisture variability, the simplified SEMB equations attribute roughly half of the variance in daily maximum temperatures found in the observations to shortwave radiation variability. Daily radiation variability is negatively skewed almost everywhere in the extratropics, and the daily shortwave radiation skewness is much better correlated with daily temperature skewness ($r = 0.49$) than monthly radiation skewness is with monthly temperature skewness ($r = 0.09$). Our results suggest that solar radiation variability driven by clouds plays an important role in the daily variability of summertime temperatures, but a fairly limited role in monthly temperature variability (section 3).

We next demonstrate that positive skewness in low-frequency temperature variability stems from (i) the long lifetime of soil moisture anomalies τ and (ii) a nonlinear relationship between soil moisture, evapotranspiration, and temperature, which ensures that a much greater temperature anomaly results from a negative soil moisture anomaly than

from an equivalent positive soil moisture anomaly (section 4). In the absence of shortwave radiation fluctuations, temperature variability is positively skewed in humid climates with infrequent dry spells and negatively skewed in dry climates with relatively infrequent precipitation (sections 5 and 6). We have shown that Z, the product of the average frequency of precipitation events ω and the drying time scale of the land surface τ, accounts for the observed time dependence in the statistical moments of temperature throughout much of the extratropics. In future work, we will examine to what extent the projected changes in heat waves due to climate change can be understood in terms of changes in these key characteristics of summertime climate.

The results of this study lead to the following hypothesis for observed extremely high summertime temperatures in the extratropics: *In all but the most arid climates, irregular and infrequent dry spells have long-lived high temperatures referred to as heat waves that are due to the combination of (i) long soil moisture memory and (ii) a nonlinear feedback between temperature and evapotranspiration via the vapor pressure deficit. Individual extremely hot days are shown to be filigree superimposed on these heat waves that are driven by state-independent high-frequency variability in solar radiation or thermal advection.* Extremely hot days are routine, high-frequency fluctuations that occur during moisture-driven, low-frequency heat waves. While this view of heat waves and extremely hot days may not be surprising, our analysis illuminates the essential feedback and physics responsible for heat waves and low-frequency summertime temperature variability, and shows that the clustering of extremely hot days in heat waves is ubiquitous in the extratropics.

APPENDIX

Statistical Moments of Shot Noise

The solution to Eq. (20) is

$$m(t) = \sum_n p_n h(t - t_n), \tag{A1}$$

where $h(t)$ is the impulse response function, and t_n are the times of precipitation events with intensities p_n. This is conventionally referred to as "shot noise" (see Papoulis 1965).

The characteristic function $\Phi(\lambda)$ is the Fourier transform of the density function; for shot noise,

$$\Phi(\lambda) = \exp\left[\int_0^\infty dp\, f(p) \int_0^\infty \omega\left(e^{ip\lambda h(t')} - 1 \right) dt' \right], \tag{A2}$$

where ω is the average rainfall frequency and $f(p)$ is the probability density function for the precipitation intensities p_n. The moment theorem relates the derivatives of the characteristic function to the central moments $\overline{m^n}$:

$$\overline{m^n} = i^n \left. \frac{\partial^n \Phi}{\partial \lambda^n} \right|_{\lambda=0}. \tag{A3}$$

Setting $h(t) = e^{-t/\tau}$ where τ is defined in Eq. (21), the first three derivatives of the characteristic function are

$$\overline{m} = i \left. \frac{\partial \Phi}{\partial \lambda} \right|_{\lambda=0} = \omega \zeta_1, \tag{A4}$$

$$\overline{m^2} = - \left. \frac{\partial^2 \Phi}{\partial \lambda^2} \right|_{\lambda=0} = \left(\omega \zeta_2 + \omega^2 \zeta_1^2 \right), \text{and} \tag{A5}$$

$$\overline{m^3} = - i \left. \frac{\partial^3 \Phi}{\partial \lambda^3} \right|_{\lambda=0} = \left(\omega \zeta_3 + 3\omega^2 \zeta_1 \zeta_2 + \zeta_1^3 \right), \tag{A6}$$

where

$$\zeta_n = i^n \int_0^\infty dp\, f(p) p^n \int_0^\infty dt'\, h(t')^n, \tag{A7}$$

$$\zeta_n = i^n \overline{p^n}\, \frac{\tau}{n}. \tag{A8}$$

We assume that the intensities of precipitation events are gamma distributed; the first three moments of the gamma distribution are given by

$$\overline{p} = p_o, \tag{A9}$$

$$\overline{p^2} = p_o^2 + p_o, \text{and} \tag{A10}$$

$$\overline{p^3} = 2p_o + 3p_o^2 + p_o^3, \tag{A11}$$

where p_o is the average precipitation intensity value. The shape parameter of the gamma distribution is set equal to one for simplicity. These moments allow us to evaluate the ζ_n values in Eq. (A8). As $\Phi(\lambda = 0) = 1$, the first three central moments of this shot noise process are

$$\overline{m} = \left. \frac{\partial \Phi}{\partial \lambda} \right|_{\lambda=0} = p_o \omega \tau, \tag{A12}$$

$$\overline{m^2} = \frac{\partial \Phi^2}{\partial \lambda^2}\bigg|_{\lambda=0} = \left(p_o + p_o^2\right)\frac{\omega\tau}{2} + (p_o\omega\tau)^2, \text{ and} \qquad \text{(A13)}$$

$$\overline{m^3} = \frac{\partial \Phi^3}{\partial \lambda^3}\bigg|_{\lambda=0} = \left(2p_o + 3p_o^2 + p_o^3\right)\frac{\omega\tau}{3}$$
$$+ \frac{3}{2}\left(p_o + p_o^2\right)(\omega\tau)^2 + (p_o\omega\tau)^3. \qquad \text{(A14)}$$

REFERENCES

Baker, M. B., H. Harrison, J. Vinelli, and K. B. Erickson, 1979: Simple stochastic models for the sources and sinks of two aerosol types. *Tellus*, **31**, 39–51, https://doi.org/10.3402/tellusa.v31i1.10408.

Berg, A., B. R. Lintner, K. L. Findell, S. Malyshev, P. C. Loikith, and P. Gentine, 2014: Impact of soil moisture–atmosphere interactions on surface temperature distribution. *J. Climate*, **27**, 7976–7993, https://doi.org/10.1175/JCLI-D-13-00591.1.

Bumbaco, K. A., K. D. Dello, and N. A. Bond, 2013: History of Pacific Northwest heat waves: Synoptic pattern and trends. *J. Appl. Meteor. Climatol.*, **52**, 1618–1631, https://doi.org/10.1175/JAMC-D-12-094.1.

Cavanaugh, N. R., and S. S. P. Shen, 2014: Northern Hemisphere climatology and trends of statistical moments documented from GHCN-daily surface air temperature station data from 1950 to 2010. *J. Climate*, **27**, 5396–5410, https://doi.org/10.1175/JCLI-D-13-00470.1.

Chan, D., A. Cobb, L. R. Vargas Zeppetello, D. S. Battisti, and P. Huybers, 2020: Summer time temperature variability increases with local warming in midlatitude regions. *Geophys. Res. Lett.*, **47**, e2020GL087624, https://doi.org/10.1029/2020GL087624.

Delworth, T. L., and S. Manabe, 1988: The influence of potential evaporation on the variabilities of simulated soil wetness and climate. *J. Climate*, **1**, 523–547, https://doi.org/10.1175/1520-0442(1988)001<0523:TIOPEO>2.0.CO;2.

Eagleson, P. S., 1978: Climate, soil, and vegetation 2: The distribution of annual precipitation derived from observed storm sequences. *Water Resour. Res.*, **14**, 713–721, https://doi.org/10.1029/WR014i005p00713.

Fernando, D., and Coauthors, 2016: What caused the spring intensification and winter demise of the 2011 drought over Texas? *Climate Dyn.*, **47**, 3077–3090, https://doi.org/10.1007/s00382-016-3014-x.

Fischer, E. M., S. I. Seneviratne, D. Lüthi, and C. Schär, 2007: Contribution of land–atmosphere coupling to recent European summer heat waves. *Geophys. Res. Lett.*, **34**, L06707, https://doi.org/10.1029/2006GL029068.

Good, E. J., D. J. Ghent, C. E. Bulgin, and J. J. Remedios, 2017: A spatiotemporal analysis of the relationship between near-surface air temperature and satellite land surface temperatures using 17 years of data from the ATSR series. *J. Geophys. Res. Atmos.*, **122**, 9185–9210, https://doi.org/10.1002/2017JD026880.

Hersbach, H., and Coauthors, 2020: The ERA5 global reanalysis. *Quart. J. Roy. Meteor. Soc.*, **146**, 1999–2049, https://doi.org/10.1002/qj.3803.

Holmes, C. R., T. Woollings, E. Hawkins, and H. de Vries, 2016: Robust future changes in temperature variability under greenhouse gas forcing and the relationship with thermal advection. *J. Climate*, **29**, 2221–2236, https://doi.org/10.1175/JCLI-D-14-00735.1.

Karlsson, K., and Coauthors, 2012: CLARA-A1: CM SAF Clouds, Albedo and Radiation Dataset from AVHRR data - Edition 1- Monthly Means/Daily Means/Pentad Means/ Monthly Histograms. Satellite Application Facility on Climate Monitoring, accessed December 2020, https://doi.org/10.5676/EUM_SAF_CM/CLARA_AVHRR/V001.

Kleidon, A., and M. Renner, 2018: Diurnal land surface energy balance partitioning estimated from the thermodynamic limit of a cold heat engine. *Earth Syst. Dyn.*, **9**, 1127–1140, https://doi.org/10.5194/esd-9-1127-2018.

Koster, R. D., and Coauthors, 2004: Regions of strong coupling between soil moisture and precipitation. *Science*, **305**, 1138–1140, https://doi.org/10.1126/science.1100217.

——, G. Salvucci, A. Rigden, M. Jung, G. Collatz, and S. Schubert, 2015: The pattern across the continental United States of evapotranspiration variability associated with water availability. *Front. Earth Sci.*, **3**, 35, https://doi.org/10.3389/feart.2015.00035.

Linz, M., G. Chen, and Z. Hu, 2018: Large-scale atmospheric control on non-Gaussian tails of midlatitude temperature distributions. *Geophys. Res. Lett.*, **45**, 9141–9149, https://doi.org/10.1029/2018GL079324.

Loeb, N. G., and Coauthors, 2018: Clouds and the Earth's Radiant Energy System (CERES) Energy Balanced and Filled (EBAF) top-of-atmosphere (TOA) Edition-4.0 data product. *J. Climate*, **31**, 895–918, https://doi.org/10.1175/JCLI-D-17-0208.1.

Loikith, P. C., J. D. Neelin, J. Meyerson, and J. S. Hunter, 2018: Short warm-side temperature distribution tails drive hot spots of warm temperature extreme increases under near-future warming. *J. Climate*, **31**, 9469–9487, https://doi.org/10.1175/JCLI-D-17-0878.1.

Manabe, S., 1969: Climate and the ocean circulation: I. The atmospheric circulation and the hydrology of the Earth's surface. *Mon. Wea. Rev.*, **97**, 739–774, https://doi.org/10.1175/1520-0493(1969)097<0739:CATOC>2.3.CO;2.

McColl, K. A., Q. He, H. Lu, and D. Entekhabi, 2019: Short-term and long-term surface soil moisture memory time scales are spatially anticorrelated at global scales. *J. Hydrometeor.*, **20**, 1165–1182, https://doi.org/10.1175/JHM-D-18-0141.1.

McKinnon, K. A., A. Rhines, M. P. Tingley, and P. Huybers, 2016: The changing shape of Northern Hemisphere summer temperature distributions. *J. Geophys. Res. Atmos.*, **121**, 8849–8868, https://doi.org/10.1002/2016JD025292.

Meehl, G. A., and C. Tebaldi, 2004: More intense, more frequent, and longer lasting heat waves in the 21st century. *Science*, **305**, 994–997, https://doi.org/10.1126/science.1098704.

Miralles, D. G., A. Teuling, C. van Heerwaarden, and J. de Arellano, 2014: Mega-heatwave temperatures due to combined soil desiccation and atmospheric heat accumulation. *Nat. Geosci.*, **7**, 345–349, https://doi.org/10.1038/ngeo2141.

——, P. Gentine, S. Seneviratne, and A. Teuling, 2018: Land–atmospheric feedbacks during droughts and heatwaves: State of the science and current challenges. *Ann. N. Y. Acad. Sci.*, **1436**, 19–35, https://doi.org/10.1111/nyas.13912.

Papoulis, A., 1965: *Probability, Random Variables, and Stochastic Processes*. McGraw-Hill, 577 pp. (see especially 554–570).

Perkins, S. E., and L. V. Alexander, 2013: On the measurement of heat waves. *J. Climate*, **26**, 4500–4517, https://doi.org/10.1175/JCLI-D-12-00383.1.

Proistosescu, C., A. Rhines, and P. Huybers, 2016: Identification and interpretation of nonnormality in atmospheric time

series. *Geophys. Res. Lett.*, **43**, 5425–5434, https://doi.org/10.1002/2016GL068880.

Rohde, R., and Coauthors, 2013: Berkeley Earth Temperature averaging process. *Geoinf. Geostat.*, **1** (2), 1–13, http://doi.org/10.4172/GIGS.1000103.

Schneider, T., T. Bischoff, and H. Płotka, 2015: Physics of changes in synoptic midlatitude temperature variability. *J. Climate*, **28**, 2312–2331, https://doi.org/10.1175/JCLI-D-14-00632.1.

Seneviratne, S. I., T. Corti, E. L. Davin, M. Hirschi, E. B. Jaeger, I. Lehner, B. Orlowsky, and A. J. Teuling, 2010: Investigating soil moisture–climate interactions in a changing climate: A review. *Earth-Sci. Rev.*, **99**, 125–161, https://doi.org/10.1016/j.earscirev.2010.02.004.

Tamarin-Brodsky, T., K. Hodges, B. Hoskins, and T. Shepherd, 2020: Changes in Northern Hemisphere temperature variability shaped by regional warming patterns. *Nat. Geosci.*, **13**, 414–421, https://doi.org/10.1038/s41561-020-0576-3.

van Heerwaarden, C. C., J. V.-G. de Arellano, A. Gounou, F. Guichard, and F. Couvreux, 2010: Understanding the daily cycle of evapotranspiration: A method to quantify the influence of forcings and feedbacks. *J. Hydrometeor.*, **11**, 1405–1422, https://doi.org/10.1175/2010JHM1272.1.

Van Weverberg, K., and Coauthors, 2018: CAUSES: Attribution of surface radiation biases in NWP and climate models near the U.S. Southern Great Plains. *J. Geophys. Res.*, **123**, 3612–3644, https://doi.org/10.1002/2017JD027188.

Vargas Zeppetello, L. R., D. S. Battisti, and M. B. Baker, 2019: The origins of soil moisture evaporation "regimes." *J. Climate*, **32**, 6939–6960, https://doi.org/10.1175/JCLI-D-19-0209.1.

——, ——, and ——, 2020a: A new look at the variance of summertime temperatures over land. *J. Climate*, **33**, 5465–5477, https://doi.org/10.1175/JCLI-D-19-0887.1.

——, É. Tétreault-Pinard, D. S. Battisti, and M. B. Baker, 2020b: Identifying the sources of continental summertime temperature variance using a diagnostic model of land–atmosphere interactions. *J. Climate*, **33**, 3547–3564, https://doi.org/10.1175/JCLI-D-19-0276.1.

Wehrli, K., B. P. Guillod, M. Hauser, M. Leclair, and S. Seneviratne, 2019: Identifying key driving processes of major recent heat waves. *J. Geophys. Res. Atmos.*, **124**, 11 746–11 765, https://doi.org/10.1029/2019JD030635.

Wilks, D. S., 2016: "The stippling shows statistically significant grid points": How research results are routinely overstated and overinterpreted, and what to do about it. *Bull. Amer. Meteor. Soc.*, **97**, 2263–2273, https://doi.org/10.1175/BAMS-D-15-00267.1.

Willmott, C., and K. Matsuura, 2018: Terrestrial air temperature and precipitation: Monthly and annual time series (1900–2017) V5.01. NOAA Earth System Research Laboratory, http://climate.geog.udel.edu/~climate/html_pages/download.html.